Understanding Ion-Exchange Processes in the Synthesis of ZnSx@ZnO1-x Heterostructures from Controlled Sulfidation of ZnO Nanocrystals

Ekaterina Bellan, Martin Jakoobi, V. Collière, Yannick Coppel, Julien Trébosc, Olivier Lafon, Pierre Lecante, Paul Fleurat-Lessard, Céline Dupont, Jean-Cyrille Hierso, et al.

Understanding Ion–Exchange Processes in the Synthesis of $ZnS_x@ZnO_{1-x}$ Heterostructures from Controlled Sulfidation of ZnO Nanocrystals

Ekaterina Bellan,[†] Martin Jakoobi,[†] Vincent Collière,[†] Yannick Coppel,[†] Julien Trébosc,[‖] Olivier Lafon,[‡] Pierre Lecante,[ß] Paul Fleurat–Lessard,[∈] Céline Dupont,[○] Jean–Cyrille Hierso,[∈] Pierre Fau,[†] Katia Fajerwerg,[†] Lauriane Pautrot–d'Alençon,[⊥] Thierry Le Mercier,[⊥] and Myrtil L. Kahn[†]*

† LCC–CNRS, Université de Toulouse, CNRS, UPS, Toulouse 31077, France

ß CEMES, UPS, Toulouse 31055, France

‖ Univ. Lille, CNRS, INRAE, Centrale Lille, Univ. Artois, FR 2638 - IMEC - Institut Michel-Eugène Chevreul, F-59000 Lille, France

‡ Univ. Lille, CNRS, Centrale Lille, Université d'Artois, UMR 8181 − UCCS − Unité de Catalyse et Chimie du Solide, F-59000 Lille, France

⊥ Solvay, Research and Innovation Centre de Paris, Aubervilliers 93308, France

∈ Institut de Chimie Moléculaire de l'Université de Bourgogne (ICMUB) UMR CNRS 6302, Université de Bourgogne (uB), 9 avenue Alain Savary, 21078 Dijon, France

○ Laboratoire Interdisciplinaire Carnot de Bourgogne (ICB), Université de Bourgogne (uB), 9 avenue Alain Savary BP 47870, 21078 Dijon, France

ABSTRACT: Semiconducting heterostructures are considered promising candidates for meeting specific environmental challenges, such as the greener or decarbonated production of energy. However, optimizing the performance of these hybrid systems largely depends on the fine understanding of the mechanisms by which they are formed, in relation to their mode of preparation. We report herein the synthesis of nanosized semiconducting heterostructures of ZnS@ZnO nature; this from well–controlled preformed ZnO nanoparticles (NPs) modified *via* anion exchange process using $(TMS)_2S$. The formation of these ZnS@ZnO heterostructures has been investigated in depth, shedding light specifically on the sulfidation mechanism and its dynamics. Our study reveals the dynamic evolution of the nanomaterial in the sulfidation process, evidencing that it is both driven by the initial presence of oxygen vacancies – acting as gateways for sulfur atoms –, and also by the action in the medium of $(TMS)_2S$, which as a sulfurizing agent behaves also as an oxygen atom extractor. The structural modification of the preformed monocrystalline ZnO nanomaterial into a polycrystalline ZnS hollow nanostructure, occurs *via* amorphization–crystallization steps, which clearly depends on the amount of $(TMS)_2S$ in the reaction. This morphological transition, from a core–shell to a hollow structure has been followed by multinuclear NMR spectroscopy (^{1}H, ^{13}C, ^{17}O), and notably oxygen atoms at the interfaces of ZnS@ZnO heterostructures have been identified and quantified. Consistently, our study clearly establishes the link between the preparation mode of the ZnS@ZnO heterostructures and the modification of their optical band gap as a function of their composition. The variation in optical properties, and the bowing of the band gap, is a function of the sulfidation level, and this mode of sulfidation is clarified step–by–step by a DFT computational approach of surface and interface processes that is fully supported by the experimental characterization (XRD, WAXS, EDX line–analysis, HRTEM, STEM–HAADF, NMR) of these materials.

INTRODUCTION

Heterostructures, i.e. semiconductor structures with specific chemical compositions exhibiting interface between two different materials with unequal band gaps,[1] hold great promises for modern needs, including green energy production,[2–4] pollution control,[5] or sensing.[6,7] Their intrinsic properties allow one to overcome the general limitations that mono–component semiconductors frequently exhibit, such as inappropriate band gap, low specific surface area, too fast charge recombination, or inappropriate redox potential.[8,9] These frequently encountered impediments can be adjusted either by band gap engineering,[10] including surface sensitization[11,12] and doping[13] with metals and non–metals, or coupling with co–catalysts.[14] All such approaches are attractive to obtain materials with controlled composition and appealing physicochemical properties.[15] Nonetheless, the chemical composition is fully dependent on the preparation protocol and thus the synthesis route impacts the heterostructure's final properties.[16,17] Consequently, a fine understanding of the relationships between the structure of such hybrid semiconducting functional materials and their applicable properties is essential.[18,19]

One of these heterostructures, $ZnS_x@ZnO_{1-x}$ (where the notation expresses the addition of the ZnS phase to the initial ZnO one) is made up of ZnO core and ZnS shell at varying O/S stoichiometries.[20–23] Different from oxysulfide phases,[24] these heterostructures have attracted increasing attention as effective, cost–efficient, and non–toxic buffer layers in thin film solar cells.[25] Additionally, in the recent years, these materials have been shown to be suitable candidates for the photocatalytic degradation of pollutants,[26] and have demonstrated to be potential candidates for clean energy production by the hydrogen evolution reaction (HER).[3,27]

Among the possible methods for the preparation of these heterostructures, chemical transformation using a preformed nanocrystal (NC) template, in which tunable ion exchange

can be conveniently employed is a very attractive route. For example, $ZnS_x@ZnO_{1-x}$ heterostructures have been previously synthesized with various sulfur sources such as H_2S,[28] $(TMS)_2S$,[29] thiourea and Na_2S,[30,31] thioacetamide,[32] and $(t\text{–}BuS)_2$.[33] These methods, based on ion exchange, mostly produced hollow nanostructures,[34] accounting for Kirkendall processes, in which the O^{2-} anions and/or Zn^{2+} cations diffuse faster outward from the ZnO NC template than the exchanged S^{2-} anions diffuse inward. A remarkable exception to these results was reported by the Cheon group, for which the use of (Z)–N–trimethylsilyloctadec–9–en–1–amine in the presence of H_2S preserved the initial structure of the semiconductor (SC). The anion diffusion through the SC could be accelerated by the assistance of an oxygen extracting reagent (OER), resulting in anion exchange without Kirkendall void formation, and thus a fairly proper conservation of the initial morphology.[28] In the latter case, the combination of the oxophilicity of the trimethylsilyl (TMS) group and the nucleophilicity of the amino group, was considered for assisting oxygen extraction, and circumvents, by a kinetic effect, the commonly encountered Kirkendall process.[35] A detailed examination of the evolution of oxygen vacancies as essential partners in the movement of ions in these structures is clearly of scientific interest and complementary to better understand these various anion–exchange synthetic approaches.

In addition to the general morphology of heterostructured NCs –and the occurrence or not of a Kirkendall process–, the optoelectronic properties should depend on the O/S composition, and thus may evolve over time according to the movements of sulfur and oxygen ions within the structure. The defects present in the $ZnS_x@ZnO_{1-x}$ material, especially the vacancies, and their propensity to facilitate atom mobility then become decisive parameters. The current literature examples regarding the synthesis of Zn–based heterostructures have succeeded in the modification of the band gap values,[36] and thereafter improved the material's optical properties.[37] Thus, starting from the same batch of NCs, semiconducting materials with different properties can be obtained depending on the post–synthesis sulfidation conditions.

Detailed knowledge of the dynamics of the oxygen and sulfur atom exchanges through available vacancies, would be a key lever to control the desired physicochemical properties for applications.

Previously, our group has developed functional metal oxide nanostructured materials using a mild organometallic synthetic approach, for their integration into devices.[38–41] The in–depth characterization of such materials, using cutting–edge techniques and notably solution and solid–state multinuclear NMR spectroscopy, has enabled us to establish pertinent links between the intimate structure and the optical properties of various semiconductor nanomaterials – including ZnO[42] and ZnS.[43] This approach paves the way to detailed exploration of hybrid ZnS@ZnO heterostructures formation from preformed ZnO NCs *via* an ionic exchange process, with a special focus on clarifying the role and fate of initial oxygen defects. We present herein a detailed study of the controlled ZnO sulfidation, both from well–defined nanorods and isotropic nanoparticles, using $(TMS)_2S$, which accompanied by Density Functional Theory (DFT) computational modeling of the process, accounts for modification of band gap values and optical properties, and establishes a comprehensive understanding of the formation of these heterostructures.

RESULTS AND DISCUSSION

Synthesis by ion exchange: structural and optical features related to sulfidation ratio

We prepared $ZnS_x@ZnO_{1-x}$ heterostructures from the sulfidation of preformed ZnO nanorods (NRs) and isotropic NPs (iNPs) obtained through hydrolysis of an organometallic precursor under mild conditions, *i.e.* at room temperature (RT) and atmospheric pressure.[44] In general, the controlled hydrolysis of the dicyclohexyl zinc complex $ZnCy_2$ leads to ZnO NCs at RT. The iNPs were obtained in THF (tetrahydrofuran) solvent in the presence of dodecylamine (DDA, 1 equiv.), while the NRs were formed from hydrolysis reaction in neat DDA (2 equiv.).

These ZnO iNPs or NRs were then sulfided in THF to give rise to $ZnS_x@ZnO_{1-x}$ heterostructures with the variable O/S ratio described in Scheme 1.

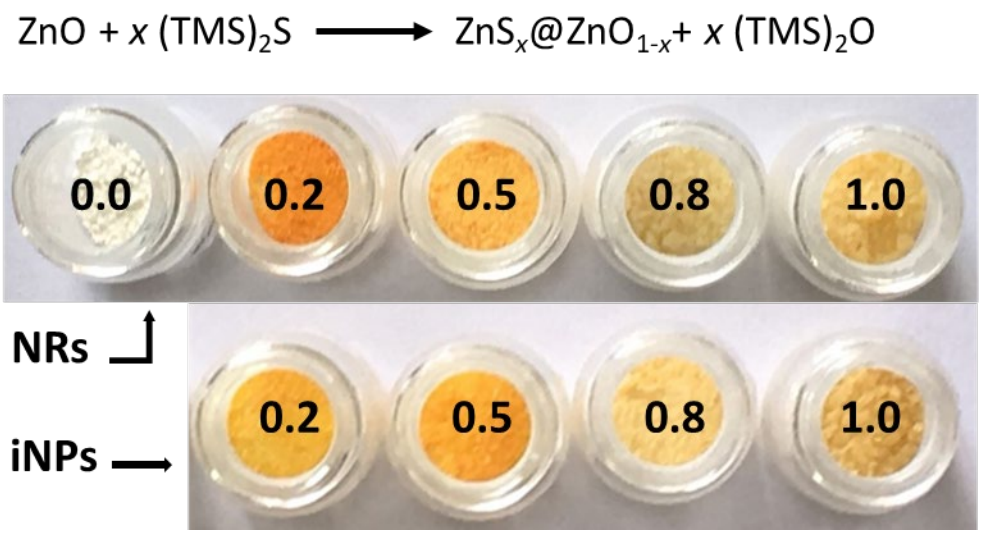

Scheme 1. Sulfidation of ZnO NCs with $(TMS)_2S$ as a function of the *x* molar equiv. of $(TMS)_2S$ added; *x* value is indicated on the images of the samples.

Taking advantage of the reactive nature of $(TMS)_2S$, the extraction of oxygen atoms from the ZnO surface led to the formation of $(TMS)_2O$, which was stable towards a reversible exchange reaction under mild conditions. Herein, for the $ZnS_x@ZnO_{1-x}$, *x* corresponds to the equivalents of $(TMS)_2S$ initially used for the sulfidation reaction. Varying the quantity of $(TMS)_2S$ with 0.2, 0.5, 0.8, and 1.0 equiv. in relation to the Zn precursor led to a color evolution of these materials, from white to orange-yellow, then pale–yellow (see Scheme 1). The measurements of optical features, performed on both colloidal solutions and in the solid state, correlated with the O/S ratio (Figures S1–S4 in the Supporting Information SI) and with the visual color. The absorbance spectra recorded in THF solution showed significant modifications depending on the $(TMS)_2S$ amount (Figures S2a and S3 (left) for NRs and iNPs, respectively). The evolution from a sharp absorbance band to a smoother one, suggests either

a change of the shape of the NRs toward iNPs or a modification of their crystallinity (*vide infra*). Additionally, the emission in the visible range was quenched regardless of the amount of $(TMS)_2S$, suggesting that all dangling bonds were removed,[45] *i.e.* that the emissive states were suppressed or at least, that these shallow surface levels became completely inactive (Figure S2a).

Moreover, measurements in the solid–state (Figure S2b for NRs, Figure S4a for iNPs) gave access to the band gap values for NRs that were found ranging from 2.9 to 3.4 eV (Figures S2c and S2d), and ranging from 3.0 to 3.5 eV (Figures S4b and S4c) for iNPs. Both sample types reached minimum values at 2.9 and 3.0 eV, respectively, at sulfidation level of 0.2 equiv. of $(TMS)_2S$ used. Such bowing of bang gap has been associated with the lattice mismatch that is related to the size and electronegativity differences between O and S atoms. This consequently leads to strain in the material, that highly depends on the sulfidation level.[36,46–48] The Urbach energy[49] increased linearly during the sulfidation process from 47 to 354 meV (Figure S2e and S2f) for NRs, and from 142 to 386 meV (Figures S4d and S4e) for iNPs, indicating that structural disorder/defect ratio augmented in the materials.

Additional powder X–ray diffraction (PXRD) measurements and radial distribution function (RDF) analysis from Wide Angle X-ray Scattering (WAXS) measurements complemented the optical measurements. Figure 1a shows the patterns of the four sulfided samples compared to a ZnO reference. The progressive disappearance of the ZnO phase, and the concomitant appearance of the ZnS phase was clearly observed.[43] As the sulfidation increased, the peaks became broader, illustrating that the crystallinity of the sample changed.[50] The broadness of the peaks associated to ZnS confirmed that the crystallite size of this phase was very small (*vide infra*).

RDF analysis of these samples showed a gradual evolution of the first peak characteristic of Zn coordination, which increased in distance from 0.19 to 0.23 nm and in amplitude (likely

because of Z difference between O and S elements) as the amount of $(TMS)_2S$ increased (Figure 1b). This observation is in good agreement with the formation of Zn–S bonds in the material since the Zn–S distance considered as the sum of the atomic radii *ca* 0.235 nm, is larger than the Zn–O distance (*ca* 0.195 nm). The intensity of the peak at 0.34 nm that was attributable to the Zn–Zn distance, decreased and a new peak appeared at 0.39 nm. The increase of the bonding Zn–X distance (X changes from O to S) was expected to induce an increase of the Zn–Zn distance. If the exchange between O and S atoms was homogeneous throughout the structure, we should observe a gradual shift in the peak associated with the Zn–Zn distance. However, we observed the disappearance of the peak associated to the Zn–Zn distance in ZnO and the concomitant appearance of a new peak. This, strongly supports a mechanistic proposal in which the sulfidation of the sample proceeded through the replacement of ZnO domains by ZnS ones. The results obtained for iNPs was consistently in line with our present explanation (Figure S5).

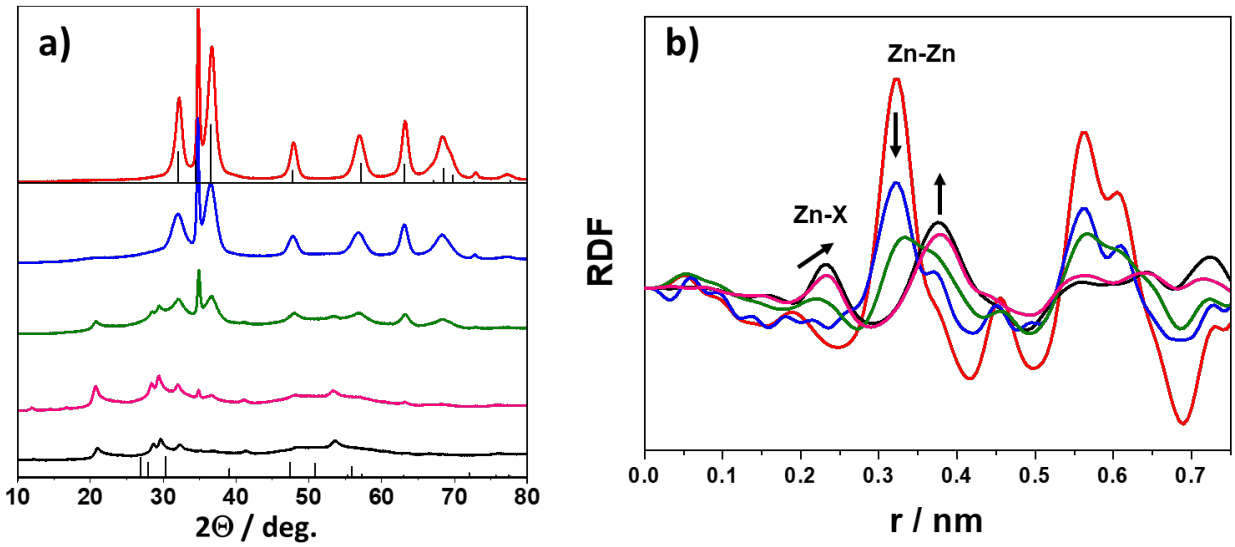

Figure 1. (a) PXRD patterns of $ZnS_x@ZnO_{1-x}$ NRs (red 0.0, blue 0.2, green 0.5, pink 0.8, and black 1.0 equiv. of $(TMS)_2S$) along with calculated diffraction patterns of crystalline ZnO and ZnS (vertical gray bars), (b) RDF diagrams for the NR samples sulfided by different amount of $(TMS)_2S$. In panel (b), X denotes O or S atom.

High resolution microscopy of $ZnS_x@ZnO_{1-x}$ and morphological modification analysis

Figure 2 shows typical TEM images of the samples. As the ratio of sulfidation agent increased from 0.2 to 1.0 equiv. the NRs, as well as the iNPs (Figure S6), clearly underwent a significant rearrangement process towards hollow structures (*vide infra*). The analysis of the size of the NRs was achieved using the 2D–size plot method, which enables the facile extraction of information on the correlation between the widths and lengths of anisotropic objects.[51] Concerning NRs, regardless of the sulfidation level, only a single sub–population was present, which indicated that the sulfidation process of the NRs did not significantly modify the global population distribution (Figures 2a and S7). Nevertheless, as the sulfidation level increased, small but noteworthy increases of both the mean width and mean length values were observed from 4.7 ± 1.1 to 6.4 ± 1.3 nm and from 45 ± 20 to 53 ± 22 nm,[52] respectively. With the increase of sulfidation level, the width and length of the NRs became significantly correlated (Pearson correlation parameter,[53] ρ, increasing from 0.23 to 0.44 after sulfidation with 1 equiv. of $(TMS)_2S$ (Figure S8), which could correspond to a simultaneous growth on both dimensions with two different but correlated speeds. Despite the fact that the distribution of NR diameters is narrow, with 95% of the rods measuring between 3.4 and 5.4 nm, it has a noticeable impact on the morphologies of the resulting heterostructures. A similar behavior was observed also for the iNPs (Figure S6). Starting from small ZnO iNPs with an average diameter of 4.1 ± 1.6 nm, a size growth up to 5.0 ± 1.6 nm was observed as the sulfidation level augmented, and the iNPs become hollow (Figure S9).

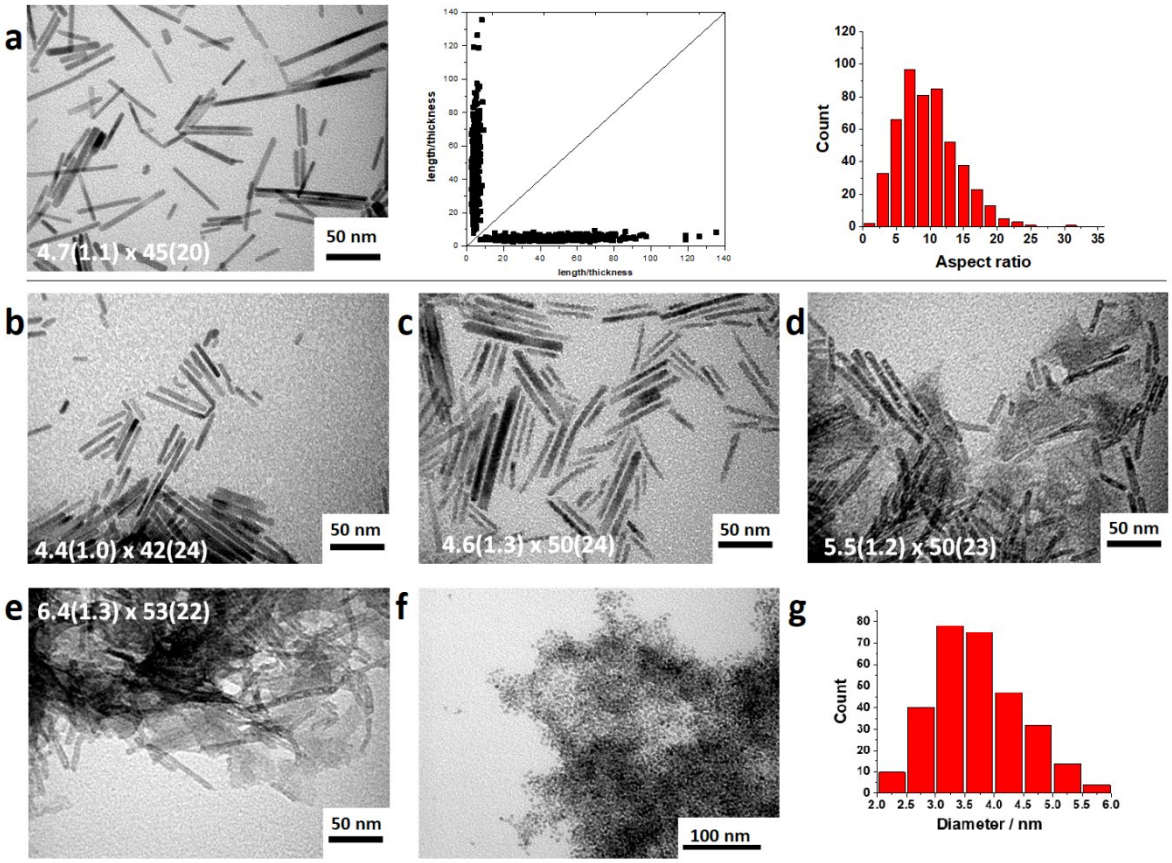

Figure 2: TEM images of $ZnS_x@ZnO_{1-x}$ NRs after 22 h of reaction with $(TMS)_2S$ (a) 0.0, (b) 0.2, (c) 0.5, (d) 0.8 and (e) 1.0 eq of $(TMS)_2S$ with mean widths and lengths along with their standard deviations indicated on the images. (f) TEM image of pristine ZnO iNPs and (g) its particle size distribution. In panel (a), the 2D–size plot and aspect ratio distributions of ZnO NRs are shown (for the other NRs see Figure S7).

Scanning Transmission Electron Microscopy – High–Angle Annular Dark–Field (STEM–HAADF) images of ZnO NRs reacted with 0.5 and 0.8 equiv. of $(TMS)_2S$ for 22 h are shown in Figure 3. For 0.5 equiv. of $(TMS)_2S$ (Figure 3a), the majority of the sample was made up of core–shell structure with a well–crystallized core and a quite disordered shell. All along the width of the ZnO NRs, few well–crystallized atomic planes were replaced by disorganized atoms. Additionally, some disruption of the pristine ZnO monocrystalline structures appeared. These areas do not present the atomic plane organization typical of an ordered structure. For 0.8 equiv. of $(TMS)_2S$ used (Figure 3b), predominantly hollow structures were observed.

However, for the larger NRs core–shell structures comparable to the one observed for 0.5 equiv. of $(TMS)_2S$ were additionally observed. Overall, as the amount of $(TMS)_2S$ increased, the number of disrupted zones increased and crystalline ZnO zones became rare as the NRs turned hollow, consistently supporting the observation of PXRD and RDF analysis. From Figure 3c, the artificially colored images were obtained by inverse fast Fourier transform of selected interatomic distances typical of either ZnO (Figure 3d) or ZnS phases (Figures 3e and S10). ZnO was clearly present only for the larger NRs, and the hollow nanorods were composed of small crystalline areas that corresponded to ZnS (Figure 3e).

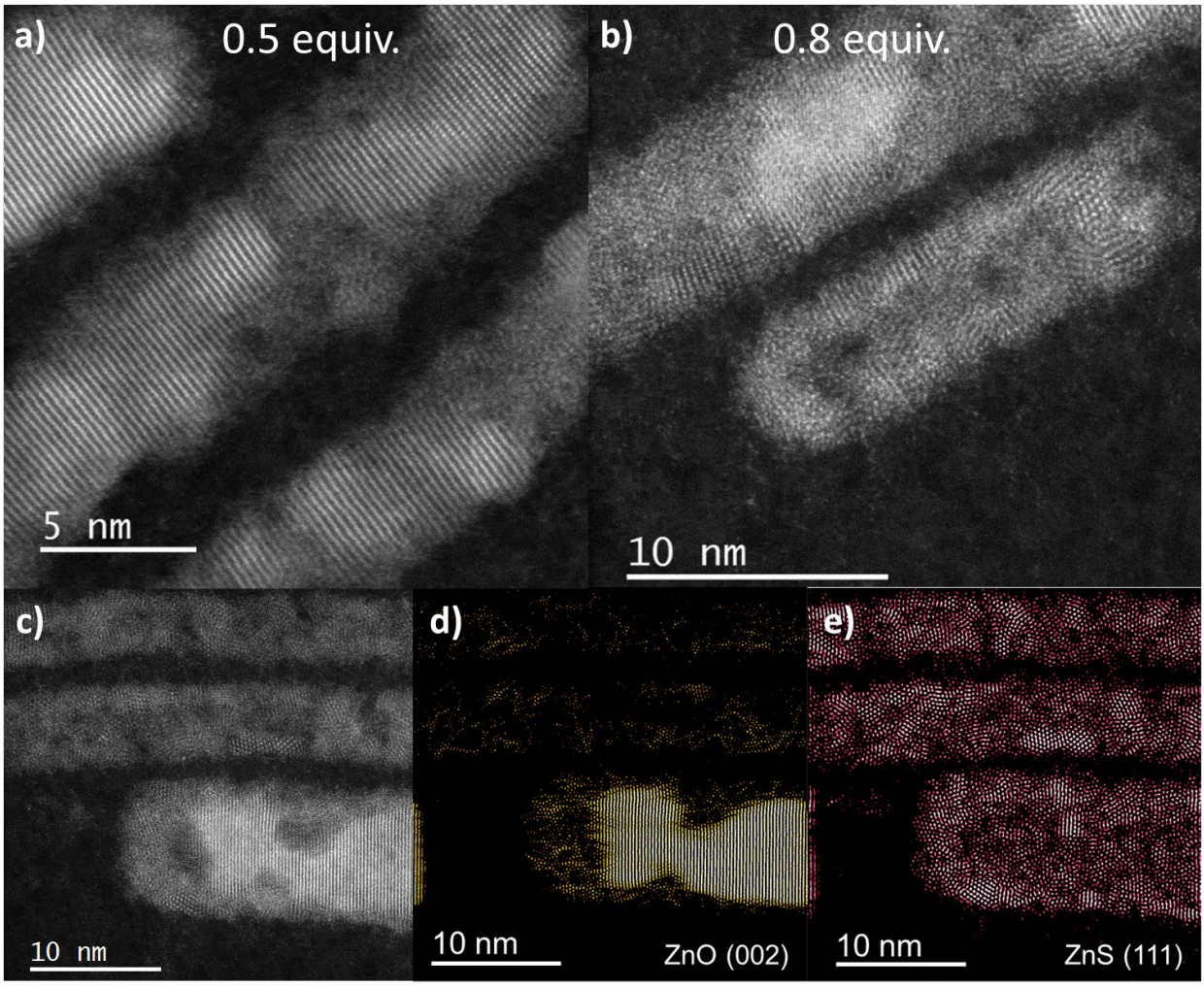

Figure 3. STEM–HAADF images of the NRs after sulfidation with (a) 0.5 equiv. and (b,c) 0.8 equiv. of $(TMS)_2S$. (c) Starting STEM–HAADF image of NRs after sulfidation with 0.8 equiv.

of $(TMS)_2S$ used to generate the colored images using inverse fast Fourier transform of selected interatomic distances characteristic of either (d) ZnO or (e) ZnS phases.

For the ZnO NRs exposed to 0.5 equiv. of $(TMS)_2S$ (Figure 4a), for which the majority of NRs are still full, the distribution profile from EDX analysis exhibited the maximum of Zn and O in the middle of the NRs and the maximum of S in the edges. For ZnO NRs exposed to 0.8 equiv. of $(TMS)_2S$, for which the majority of NRs are hollow, the Zn and S distribution profile clearly evidenced that Zn and S atoms were more abundant in the shell nearest to the cavity (Figure 4b). Similar results were obtained for iNPs (Figures 4c, 4d, and S12).

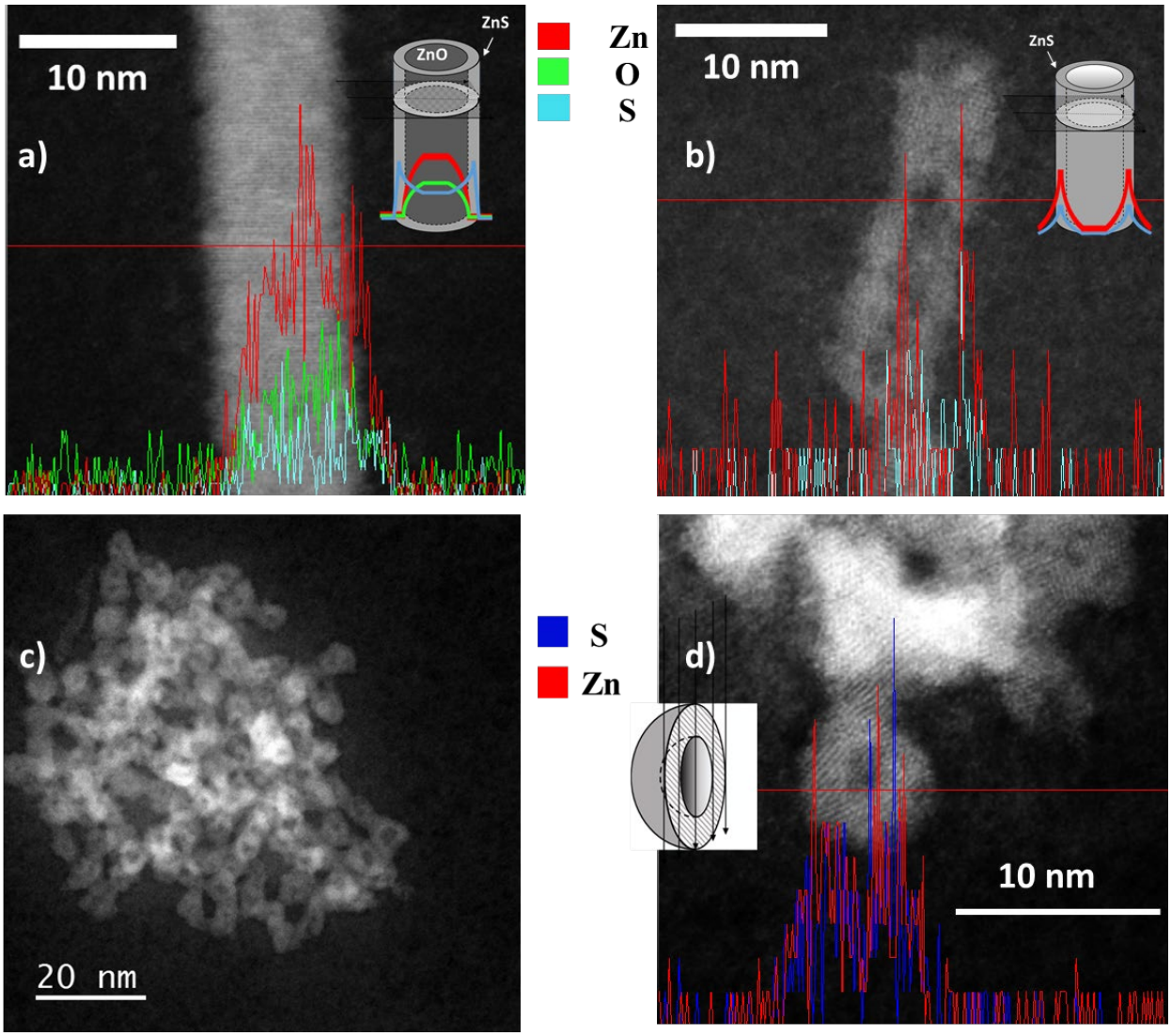

Figure 4. STEM–HAADF images of (a, b) NRs and (c, d) iNPs after sulfidation by 0.5 (a and c) and 0.8 equiv. (b and d) of $(TMS)_2S$. EDX line analysis on single nano–object is displayed in panels (a, b, and d).

The formation of the hollow structures was also followed over time for ZnO NRs sulfided with 0.8 equiv. of $(TMS)_2S$ (Figure S13). TEM images recorded from $t = 0$ to $t = 96$ h showed that the change in the morphology typically started after 20 min. The formation of holes in some NRs was observed after 1 h of reaction, and some hollow NRs were observed after 22 h. After 96 h, all the NRs had transformed into hollow structures. Note that the sulfidation of the NRs seems to depend on the width of the pristine ZnO NRs and not on their length (see Figure S14 and the respective discussion). The size distribution of the diameter of the pristine ZnO NRs can lead to the presence of both full and hollow structures depending on the amount of sulfuring agent and the reaction time. The simultaneous presence of these structures in the samples for at least 0.5 equiv. of $(TMS)_2S$ (and higher) allows us to hypothesize that the stages of the sulfidation process remain identical whatever the diameter of the NRs. We can thus equate these different structures with different degrees of advancement in the sulfidation process. This provides a means to visualize the time-evolution of the sulfidation mechanism.

Mechanism of the $ZnS_x@ZnO_{1-x}$ hollowing rearrangement process

As shown by STEM–HAADF, the formation of $ZnS_x@ZnO_{1-x}$ heterostructures by exchange of oxygen for sulfur atoms in monocrystalline ZnO NCs proceeded through the initial formation of compact zones of disorganized ZnS phases, which then gradually changed into hollow polycrystalline ZnS structures.[3,5,54]This progressive structural transformation was complete after 96 h for 1 equiv. of $(TMS)_2S$, giving a full population of polycrystalline ZnS hollow structures. However, some patchwork structures containing adjacent ZnO and ZnS domains could be obtained when smaller amounts of sulfurizing agent were employed,

providing an interesting lever of structural control. As this exchange of atoms is a dynamic process, the final ratio of sulfidation also depends on the reaction time. Consistently, the formation of hollow structures by anionic exchange can be postulated *via* a mechanism analogous to void formation due to the Kirkendall effect.[30,55]

Nonetheless, the sulfidation of anisotropic ZnO NRs raised some important and specific key points about this anionic exchange phenomenon. As illustrated in Scheme 2, the sulfidation occurred from the surface to the core of the NRs and preferentially started at the surface defects, as demonstrated in ref 34. Core–shell structures could be obtained in the early stages of the sulfidation reaction regardless of the quantity of $(TMS)_2S$, or alternatively for a small amount of extracted O–atoms (Scheme 2a). However, as such defects were not uniformly distributed along the NRs, the formed structural patchwork pattern varied from one NR to another. In turn, the voids in the structure (Scheme 2b) –formed by the co–diffusion of the Zn and O–atoms induced by the formation of the ZnS phase– were distributed differently in each of the NRs. The amorphization of the material, due to the lattice mismatch between oxygen and sulfur ions led to the final hollow structures with ZnS crystalline domains of limited size (Scheme 2c).

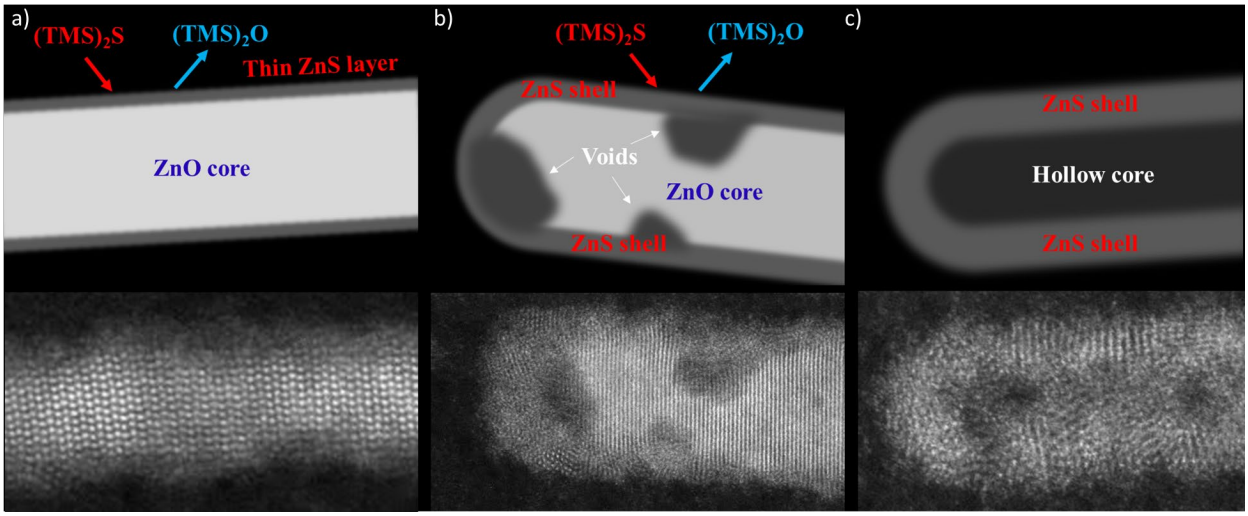

Scheme 2. Mechanistic approach for the sulfidation of ZnO NRs by $(TMS)_2S$ highlighting formation of voids and amorphization of the NRs due to difference in the kinetic of O– and S– atom migration.

Probing local environments of O atoms in $ZnS_x@ZnO_{1-x}$ using NMR

In order to gain additional information on chemical environments and local structure in $ZnS_x@ZnO_{1-x}$ heterostructures, particularly at the interface of the domains, we carried out multinuclear NMR experiments. These are suitable for fine probing materials at the atomic level, notably in NPs.[56] Relative to such nano–objects, the use of NMR provides information concerning both the interactions between surface ligands and the core, as well as concerning the very structure and intimate arrangement of the inorganic nano–object core.[43,57–59]

We first used $^1H \rightarrow ^{13}C$ cross-polarization magic–angle spinning (CP-MAS) NMR experiments to monitor the surface state of the samples at the molecular scale. We previously demonstrated that DDA alkyl chains adopt zig–zag conformation with a majority of *trans-trans* (*tt*) configurations in pure ZnS NRs.[18] Conversely, DDA long–chains exhibit highly disordered conformation with mainly *trans–gauche* (*tg*) configurations when interacting with ZnO.[57] This difference in conformation arose from the existence of hydrogen bonds between H-atoms in the DDA alkyl chain and O–atoms on the ZnO surface, which no longer existed with the less electronegative sulfur atoms. Advantageously, the *tt* (ZnS) or *tg* (ZnO) configurations result in distinct ^{13}C isotropic chemical shifts of the central CH_2 groups of DDA's aliphatic chain at *ca.* 30 and 32 ppm, respectively.[43,57] For NR samples sulfided with 1.0, 0.8, 0.5, and 0.2 equiv. of $(TMS)_2S$, respectively, *tt/tg* ratios of 85/15(±5), 70/30(±5), 50/50(±5), and 20/80(±5) were measured (Figure S15), assuming similar $^1H \rightarrow ^{13}C$ CP-MAS transfer efficiency for both configurations.[60] The *tg*/*tt* ratio associated with the presence of ZnS and ZnO zones on the surface of nano–objects demonstrated a linear dependence on the amount of $(TMS)_2S$ and is

therefore a reliable marker for quantifying the level of sulfidation (Figure S16). Similar results were obtained for iNPs (Figures S17 and S18).

The use of ^{17}O NMR is also particularly interesting for oxide nanomaterials characterization. For instance, this powerful approach has enabled the characterization of the different phases present in aluminum–doped ZnO NPs, such as complex $ZnAl_2O_4$ spinel[61] and allowed the observation of O vacancies near the surface of ZnO NPs.[62] Very recently, ^{17}O solid state NMR spectroscopy was successfully coupled with DFT calculations to study the surface structure of ZnO NRs and explore the H_2 activation process.[63] Some of us have also shown that ^{17}O–atoms from labelled water molecules were incorporated into ZnO NPs by diffusing from the surface to the NPs core.[58] We thus envisioned that quantitative information on the sulfidation kinetics could thus be obtained by ^{17}O NMR.

^{17}O–enriched ZnO ($Zn^{17}O$) NRs were prepared using $H_2{}^{17}O$ for the controlled hydrolysis reaction. Figure 5 shows ^{17}O MAS NMR spectra of these $Zn^{17}O$ NRs when exposed to $(TMS)_2S$ over time.

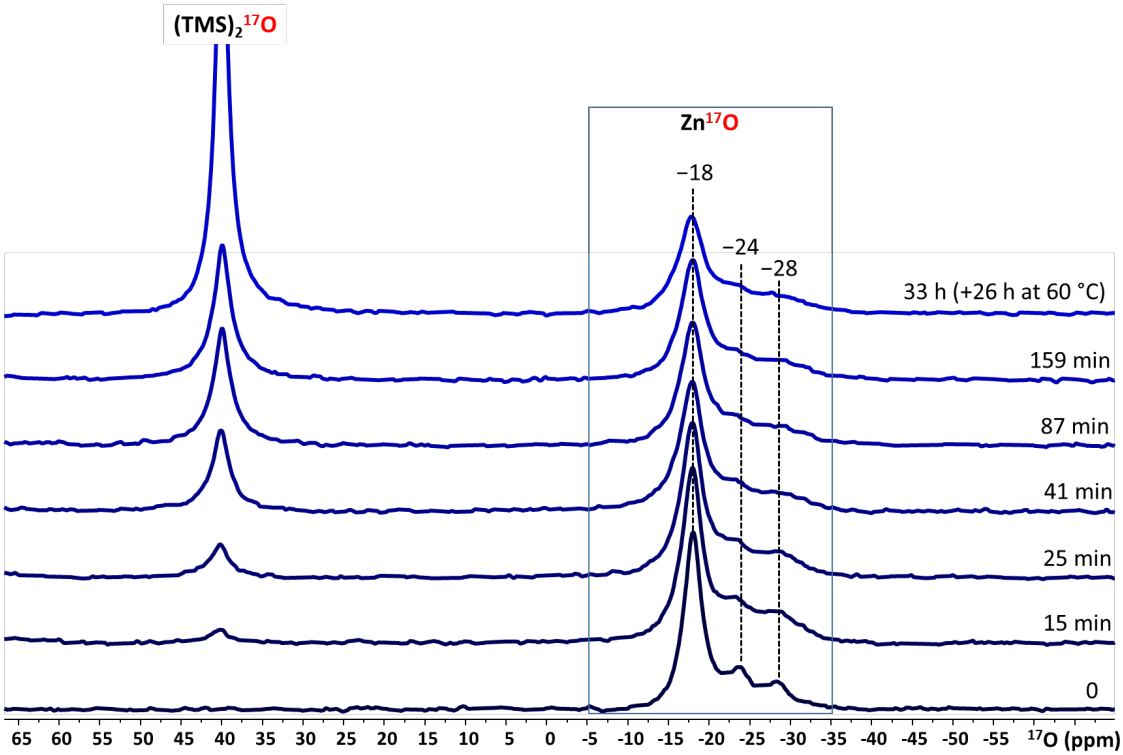

Figure 5. Evolution of 1D ^{17}O MAS NMR spectra acquired at 9.4 T with ν_R = 8 kHz over time of the sulfidation of Zn^{17}O NRs in–situ by an excess of $(TMS)_2S$.

Clearly, an increase of the ^{17}O signal at 40 ppm characteristic of $(TMS)_2{}^{17}O$ together with the decrease of the typical ^{17}O ZnO signals between -18 and -30 ppm were observed over time. Such monitoring clearly characterized the anion exchange process, and we extracted various quantitative information from those data by normalizing the respective variation of the three peaks over time (Figure S19). Notably, the peaks at -24 and -28 ppm attributed to respectively the surface and near–surface O–atoms in ZnO,[58] have consistently similar kinetics of evolution with a half–reaction time for sulfidation of *ca.* 20 min. Conversely, the signal at -18 ppm that was associated to the core O–atoms (in–depth ZnO layers) underwent a clearly slower evolution with *ca.* 30 min of half–reaction time for sulfidation. In addition, a higher level of sulfidation exchange was observed for the O–atoms at the surface estimated at *ca.* 70% against *ca.* 55% for the core–O–atoms. Consistent kinetic data were obtained when fitting the evolution over time of TMS peak of the $^{17}O(TMS)_2$ both in ^{1}H and ^{17}O MAS NMR spectra over time (Figures S20–S22).

These in–situ experiments did not reveal new ^{17}O signals that may be associated with specific oxygen atoms at the interface between the ZnO and ZnS domains. With the view to eventually detecting such interfacial specific ^{17}O environments arising upon the formation of ZnS@ZnO heterostructures, we explored ^{17}O isotopic exchange experiment on preformed $ZnS_x@ZnO_{1-x}$. We thus reacted $ZnS_x@ZnO_{1-x}$ (x = 0.2 to 0.8 equiv.) with ^{17}O–enriched water at RT. No ^{17}O signals were observed after 24 hours which suggested that for stabilized sulfided heterostructures, reverse exchange of sulfur for oxygen, or even oxygen for oxygen, was not achieved, all the more in the absence of O–extractant. However, by heating the sample at 60 °C for 72 h, ^{17}O could be incorporated into the material in various amounts. Figure 6 shows the 1D ^{17}O MAS NMR spectra obtained at high magnetic field (18.8 T) of ZnO iNPs sulfided with

0.2, 0.5 or 0.8 equiv. of $(TMS)_2S$, and then further reacted with ^{17}O for isotopic exchange using $H_2{}^{17}O$ at 60 °C during 72 h.

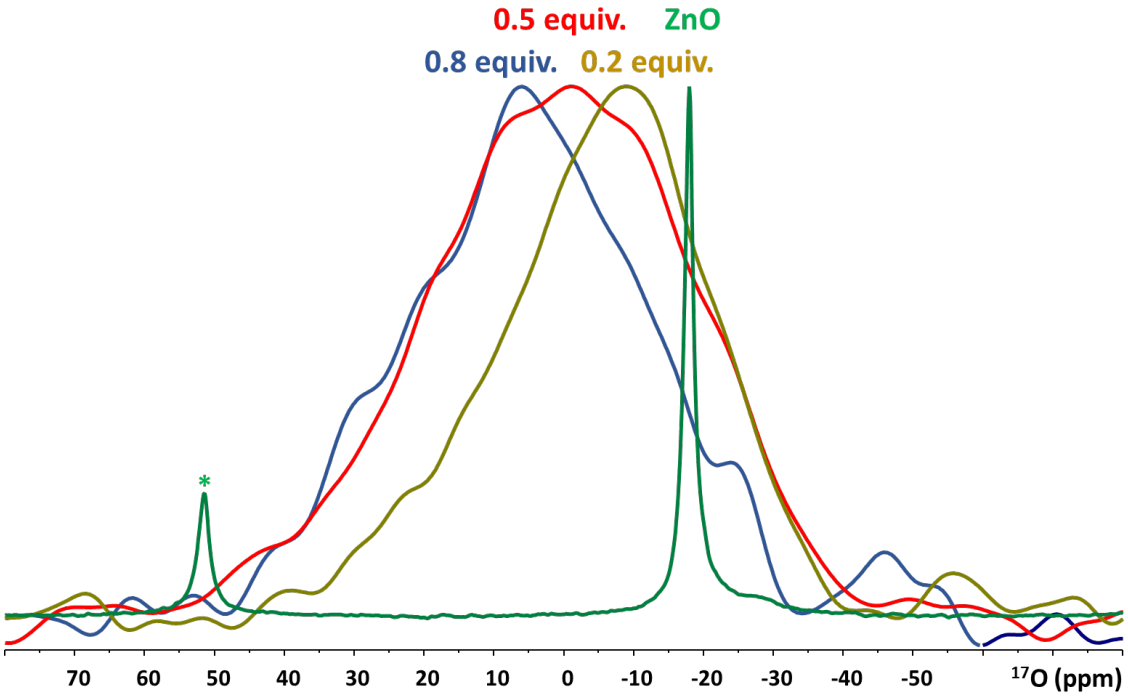

Figure 6. 1D ^{17}O MAS NMR spectra at 18.8 T (ν_R = 14.26 kHz) of $Zn^{17}O$ iNPs (green) and ZnO iNPs sulfided by 0.2, 0.5 and 0.8 of $(TMS)_2S$ and then exposed to $H_2{}^{17}O$ for 72 h at 60 °C, followed by drying under vacuum to remove residual ^{1} $H_2{}^7O$ molecules. The intensity of the spectra was set at the same level to better highlight variations in chemical shifts. The symbol * denotes spinning sidebands associated to the ZnO signal at -18 ppm.

The ^{17}O NMR spectrum of $Zn^{17}O$ iNPs, which were enriched in ^{17}O isotope during the synthesis, is dominated by the signal of O sites in the core region. This signal is narrow owing to the high octahedral symmetry of the O atoms, which results in small quadrupolar coupling constant, $C_Q \approx 0.2$ MHz.[64] The ^{17}O NMR spectra of sulfided ZnO iNPs, which were enriched after sulfidation by exposure to $H_2{}^{17}O$, are much broader than that of $Zn^{17}O$ iNPs. These NMR spectra are also broader than those of ZnO iNPs, which were exposed to $H_2{}^{17}O$ after their

synthesis and are selectively enriched in ^{17}O isotope near their surface.[58] Hence, the observed broadening does not only result from increased electric field gradient and broader distribution of local environment near surface of nanoparticles[62] but portrays increased disorder [65] produced by sulfidation. This observation is consistent with the loss of crystallinity observed by PXRD and STEM. As the amount of $(TMS)_2S$ increased, the peaks maxima shifted to higher frequencies. Chemical shifts of -6.7, -0.2, and 4.9 ppm were measured for sulfidation using 0.2, 0.5 and 0.8 equiv. respectively, which can be compared to the -18 ppm shift observed for core oxygen in pure ZnO iNPs. This evidences a significant change in the environments of the O–atoms exchanged with $^{17}OH_2$.

^{17}O multiple–quantum magic–angle spinning (MQMAS) experiment performed on $ZnS_{0.2}@ZnO_{0.8}$ showed the presence of at least two groups of oxygen atoms, with significantly different quadrupolar constants of about 1 MHz and 5 MHz. They both present a large chemical shift distribution (Figure S23), which evidenced the structural heterogeneity of the material. 1D ^{17}O spectra obtained at 9.4 and 18.8 T were simulated simultaneously (Figure S24 and Table S1. For the three samples, no satisfactory agreement between experimental and simulated spectra was achieved when considering a single ^{17}O site. Conversely, reasonable agreement was obtained when considering two sites with parameters similar to those determined for $ZnS_{0.2}@ZnO_{0.8}$. This observation suggests that the three investigated samples contain at least two different sites **A** and **B** with broad chemical shift distribution. The complete orientational averaging of chemical shift tensors, *i.e.* the isotropic chemical shift, of site **A** had a positive value ($3.0\ ppm \leq \delta_{iso}(^{17}O) \leq 34.0\ ppm$) with large quadrupolar coupling constant, $C_Q \approx 5$ MHz, while site **B** had negative shifts ($-10.0\ ppm \leq \delta_{iso}(^{17}O) \leq 0.0\ ppm$) and weak $C_Q \approx 1.5$ MHz. Site **B** had δ_{iso} and C_Q values slightly higher than those of ^{17}O nuclei of ZnO (i. e. −18.0 ppm with $C_Q \leq 1.0$ MHz) and could probably be associated with ^{17}O diffusion within the residual ZnO phases. Site **A** corresponded to a new environment around oxygen, not observed for ZnO,

and may correspond to O at the interface of the ZnO and ZnS domains since the S/O level of substitution increases both δ_{iso} (as seen in Figure 6) and C_Q, by reducing the local symmetry around ^{17}O nuclei. We can notice that some experimental spectra shown in Figures S23 and S24 slightly deviate from those simulated using two sites for large shift values. This deviation could indicate the presence of additional ^{17}O local environments, such as those in proximity of O vacancies.[62]

Additional structural data about the interface were obtained by using $^{1}H \rightarrow ^{17}O$ 2D PRESTO NMR experiments focusing on interactions between exchanged ^{17}O nuclei and the ^{1}H–containing species. Close spatial proximities between O and H atoms were observed both in the range 0.9 to 2.7 ppm and up to 7.0 ppm that were characteristic of the aliphatic chains of the DDA ligands and of hydroxyl groups, respectively (see Figure 7). ^{1}H signals above 3.0 ppm, corresponding to OH groups, were mainly linked to the most deshielded ^{17}O signals. The intensity of these correlations indicated that the proportion of OH groups at the interface was significant for all sulfidation levels.

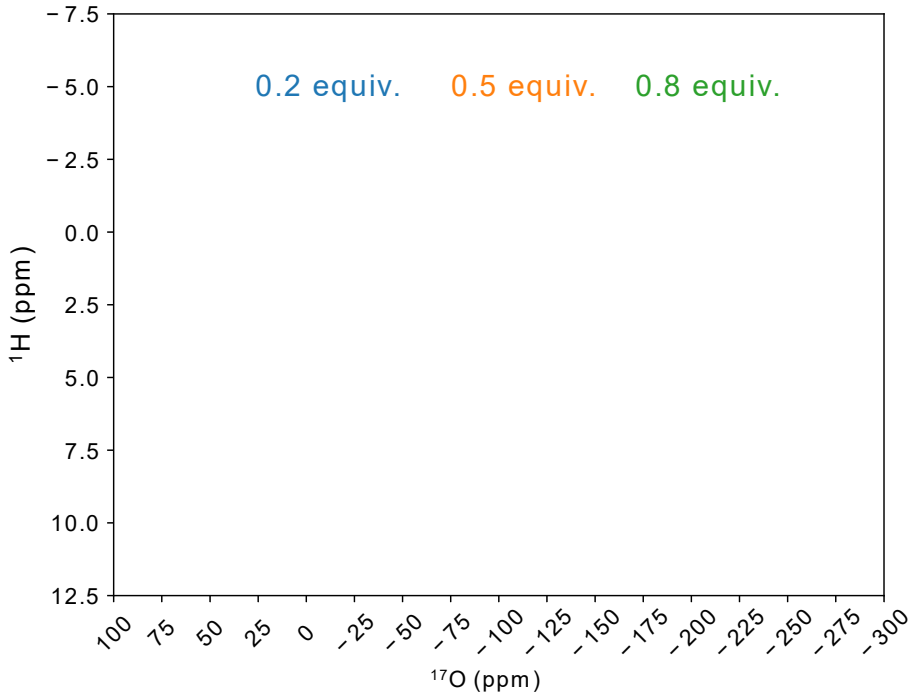

Figure 7. $^{1}H \rightarrow {}^{17}O$ 2D PRESTO MAS NMR spectra (at 18.8 T, ν_R = 14.26 kHz) of $Zn^{17}O$ iNPs sulfided by 0.2, 0.5, and 0.8 equiv. of $(TMS)_2S$.

We previously reported a partial reversibility of the $^{16}O/^{17}O$ isotopic exchanges for both NRs and iNPs of ZnO formed under analogous conditions, a reversibility which was associated with some surface reconstruction process.[58] The occurrence of such reversibility phenomenon was also checked for the $ZnS_x@ZnO_{1-x}$ heterostructures described herein by recording the ^{17}O MAS spectra of the samples reacted first with ^{17}O–enriched water during 72 h at 60 °C (step 1), then with unenriched water (step 2) and finally with ^{17}O–enriched water again (step 3) (Figure S25). Regardless of the level of sulfidation, the evolution of the spectra was the same. When a labelled sample was exposed to unlabeled water (from step 1 to step 2), a decrease in signal intensity was observed evidencing that most of the O species were reversibly exchanged. When the sample was then exposed to labelled water (step 2 to step 3), the signal intensity

increased but did not return to its initial level (step 1) showing that a fraction of the $^{16}O/^{17}O$ atoms were nonexchangeable.

The quantification of these isotopic exchanges by integration of the recorded signals showed that 63(±5), 53(±5) and 86(±2) % of the initial signal was lost between step 1 and step 2 after sulfidation with 0.2, 0.5, and 0.8 equiv. of $(TMS)_2S$, respectively. After step 3, 61(±4), 91(±8) and 88(±8) % of the initial signal recorded in step 1 was recovered. This result indicates a dynamic restructuration of the material that can be related to a diminution of the vacancies in ZnS@ZnO starting material, as has already been observed for ZnO NCs.[58] For 0.5 equiv. (and above) of sulfuring agent, the exchange appears almost totally reversible which means that nearly no non-exchangeable O is incorporated. This suggests that there is little or no crystalline ZnO left to absorb O–atoms to fill the vacancies, which agrees with the RDF analysis where the material is highly amorphous. Importantly, simulation of the 1D ^{17}O MAS NMR spectra (Figure S25) of the residual ^{17}O–atoms (step 2) of $ZnO_{0.8}@ZnS_{0.2}$ and $ZnO_{0.5}@ZnS_{0.5}$ heterostructures allowed the quantification of the site **A** and site **B** contents that were of 66(±6) and 82(±6)% for site **B** (ZnO part) and of 21(±4) and 42(±5)% for site **A** assumed to be at the interface, respectively. The oxygen atoms of the interface were more easily exchanged with oxygen atoms of water than the oxygen atoms of the residual ZnO area.

The ^{17}O NMR analysis combined with the HR–TEM monitoring over time highlighted important aspects concerning the sulfidation mechanism of ZnO NPs towards well–controlled $ZnS_x@ZnO_{1-x}$ heterostructures, which represents a breakthrough in understanding the link between the preparation mode of these heterostructures and their related specific band gap and optical properties. We assume that the oxygen vacancies initially present serve as preferential gateways for the incoming S–atoms. Since oxygen vacancies are associated with zinc atoms embedded in an undercoordinated surrounding, the formation of Zn–S bonds more easily completes the coordination sphere of these Zn ions. The presence of O–vacancies constitutes,

thus, a powerful driving force of the sulfidation process. Consequently, a decisive issue for controlling the synthesis of heterostructures from ZnO nanomaterial template via anion exchange–process is the identification and quantification of these vacancies. In that respect, the results described herein evidence the presence of vacancies can be advantageously highlighted by isotopic exchange between the O–atoms of water and those of the ZnO.

Computational approach of surface processes

Complementary to the existence of native O–vacancies, their formation during sulfidation process was boosted by the oxophilicity of the TMS group that favored the formation of hexamethyldisiloxane $(TMS)_2O$ through the creation of strong Si–O bonds. This was confirmed by quantifying the oxophilicity of the trimethylsilyl group through computation of the Gibbs free energy for the model reaction of $(TMS)_2S$ with water, to give $(TMS)_2O$ and H_2S (see SI for computational details). The high exergonicity of $\Delta_r G^0$ = -33.6 kcal mol^{-1} found supports $(TMS)_2S$ role as a strong O–atom extractor (Scheme 3). Formation of $(TMS)_2O$ acts as a second driving force in the sulfidation process, which will continue to take place, as long as residual $(TMS)_2S$ is present in the medium.

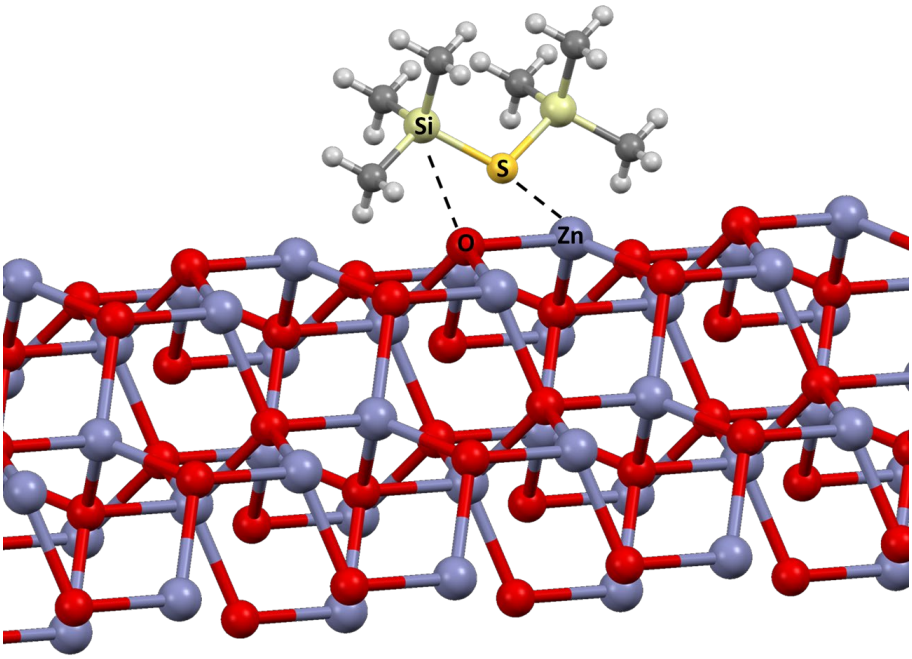

Scheme 3. Schematic proposal for approaching concerted sulfidation process of ZnO into ZnS using $(TMS)_2S$.

Scheme 4 illustrates a proposal for stepwise transformation of ZnO NRs into ZnS NRs *via* the ZnS@ZnO phases that is also applicable to ZnO iNPs. This enables the evolution of the material's physical properties and in particular, allows one to link the evolution of the band gap values to the structural modifications throughout the sulfidation process.

The reaction with $(TMS)_2S$ of plain (nonhollow) ZnO NRs, having a stable given length and width and a given band gap value, triggers the sulfidation process (Scheme 4a). For the sulfidation to proceed, oxygen vacancies allow easier diffusion pathways for sulfur ions to move further toward the core and bind undercoordinated zinc ions. The vacancies are also obviously necessary for the oxygen ions to move towards the surface for continuous extraction. This global movement of the anionic sub–lattice induces rearrangement of the cationic sub–lattice. Such movements take place at the atomic scale, generating strains within the material that is amplified by the lattice mismatch between ZnO and ZnS domains; the vacancies contributing to relieve this strain.

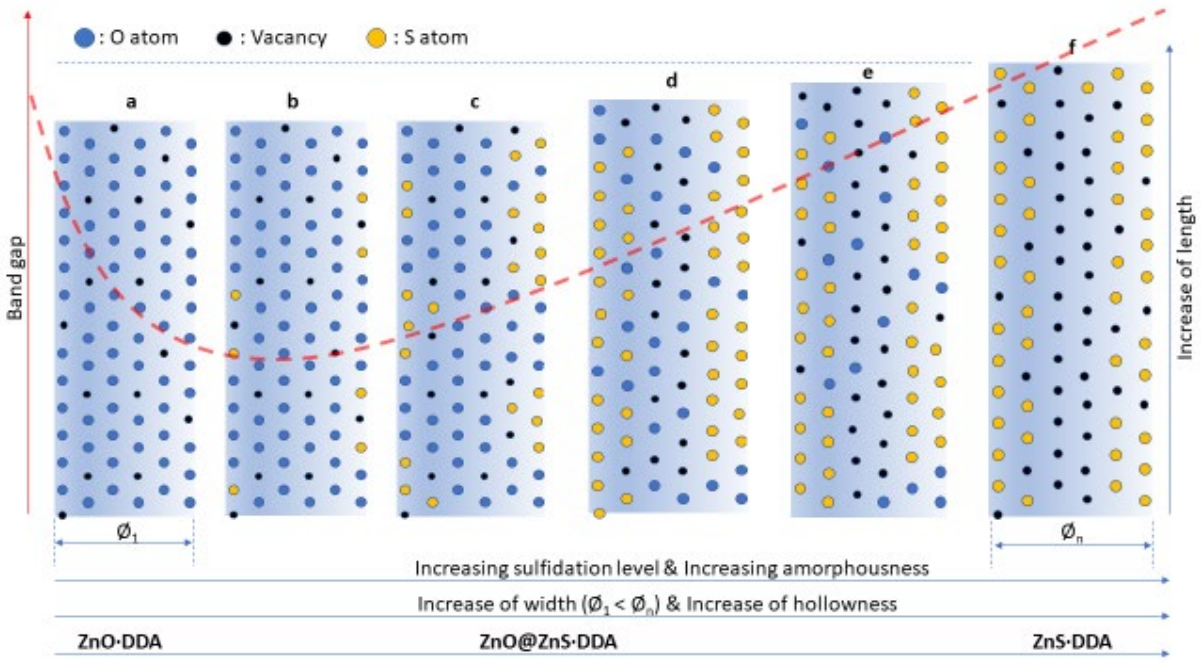

Scheme 4. Monitoring of crystallinity, band gap, width/length and hollowness of ZnO NRs evolving upon sulfidation first to core-shell ZnS@ZnO heterostructures then to hollow ZnS NRs. The red dash line indicates the changes in the band gap value.

At the beginning of the sulfidation process, and equally at low $(TMS)_2S$ reagent level, the exchanges between oxygen and sulfur atoms take place using the vacancies of these lacunar ZnO NPs. Initial ZnO/ZnS interfaces would be formed, leading to an overall structure containing a patchwork of ZnO crystallites smaller than that of the initial material. This results in an abrupt decrease of band gap (Scheme 4b). These progressive dynamic movements at atomic scale induce further loss of chemical order corresponding to the visible amorphization of the nanomaterial. When the sulfidation process is prolonged in time, and equally using higher quantity of $(TMS_2)S$, the migration of the atoms leaves behind voids or void–like patches (see Scheme 4c–e). This highlights a significant O–vacancy density in the initial ZnO, and agrees with the observed initial optical features and recent NMR measurements[62] (*vide supra*). The active migration from the core to the shell of the NCs is consistent with the driving forces described above, notably related to the formation of strong Si–O bonds, which will continue to take place as long as $(TMS)_2S$ remains in the reaction. We also performed the ZnO NCs sulfidation using H_2S, from which the oxygen extractor properties demonstrated by $(TMS)_2S$ were comparatively absent, as shown by the absence of final hollow nanostructures (Figure S26).

As the sulfidation level increases, the initially formed amorphous ZnS areas evolve to crystalline phase (Scheme 4c–4e). This structural rearrangement leads to a gap widening that is attributed to the transition from a sulfur–doped ZnO material to an oxygen–doped ZnS. Reaching the highest sulfidation level is correlated to the global hollow structure formation of ZnS (Scheme 4f), which is made of a patchwork of compact ZnS crystallite areas that overall exhibit a band gap value lower than the one of a ZnS bulk material. Notably, throughout this

sulfidation process, the diffusion of the ions and the exchange of O– for bigger S–ions induces an increase of the length and width of the initial NRs (see Scheme 4), correlated by HR–TEM monitoring. This non–monotonous evolution of the gap has a direct consequence on the color of the NP and NR (depicted in Scheme 1): the initial ZnO material is white because its gap of 3.4 eV is greater than the visible domain (between 1.6 and 3.2 eV). For sulfur content less than 0.2 equiv., the gap decreases below 3.0 eV (see SI) and the material becomes orange-yellow. Then, as the sulfur content increases, the gap starts increasing, and the color fades.

To correlate these results, model DFT calculations that support this detailed mechanistic approach were carried out (see SI for computational details). Firstly, band gaps were determined for the $(10\bar{1}0)$ surfaces of both reference compounds, namely ZnO and ZnS, leading to respective values of 2.14 and 3.21 eV. Starting from the ZnO$(10\bar{1}0)$ surface, S–atoms have been progressively added to simulate the experimental increase of sulfidation level (from 1 up to 7 S-atoms, which corresponds to sulfidation level of 3.12 to 21.87 %). For each level, optimization was performed to determine the most stable sulfur position. Steadily, the sulfidation occurs in the surface layers and evolves gradually towards deeper layers (see in Figure S27 most stable structure for each sulfidation level). This fully agreed with NMR results indicating a sulfidation evolving from surface to core with different kinetics (see Figure 5). Additionally, the changes in band gaps were calculated depending of the sulfidation levels and are gathered in Figure 8.

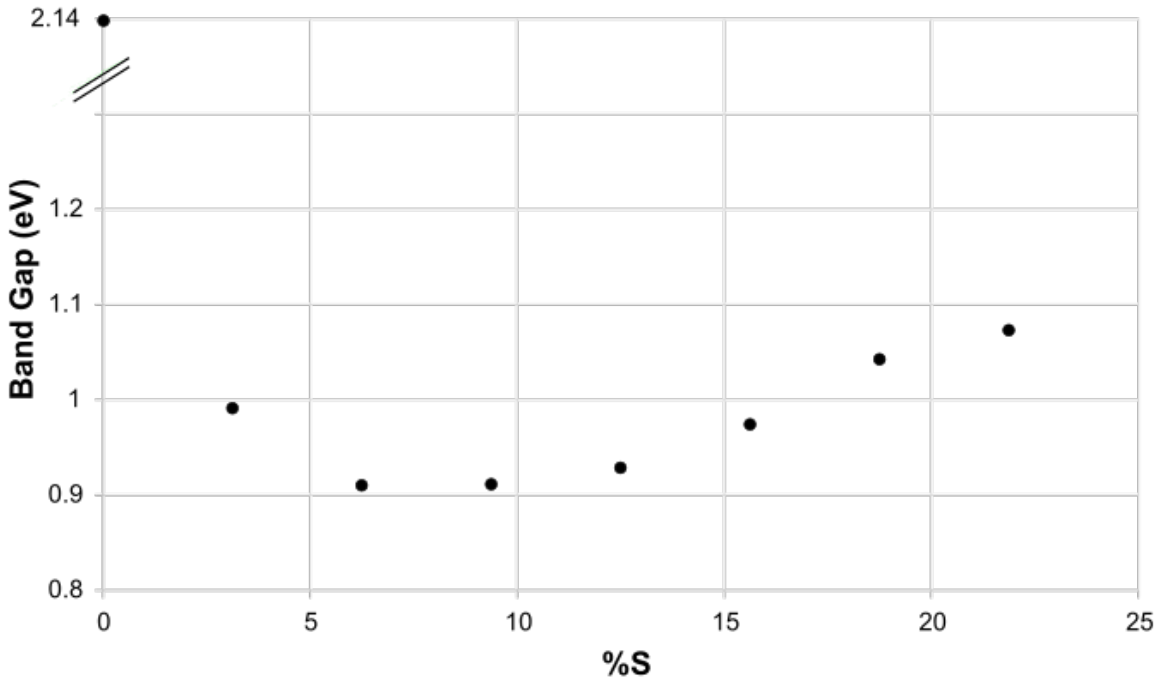

Figure 8. Calculated band gap evolution (in eV) as a function of the sulfidation level (in atom% of S).

Computational results satisfactorily reproduce the trends of experimental changes of band gap, with a minimum value reached for sulfidation levels ranging between 5 and 10 atom%. This data thus gives an approximate evaluation of the atomic incorporation with 0.2 equiv. of $(TMS)_2S$. The narrowing of band gap in the presence of sulfur can be interpreted from density of states (DOS) calculations. DOS for pure ZnO compared to those in the presence of 6.25 atom% of sulfur are reported on Figure 9. When comparing DOS of pure ZnO and $ZnS_x@ZnO_{1-x}$, the narrowing of the gap is clearly visible (see black lines). The projection of DOS on the S 3p states confirm their presence in the gap, and thus the direct involvement of sulfur atoms in the narrowing of band gap observed for sulfided samples.

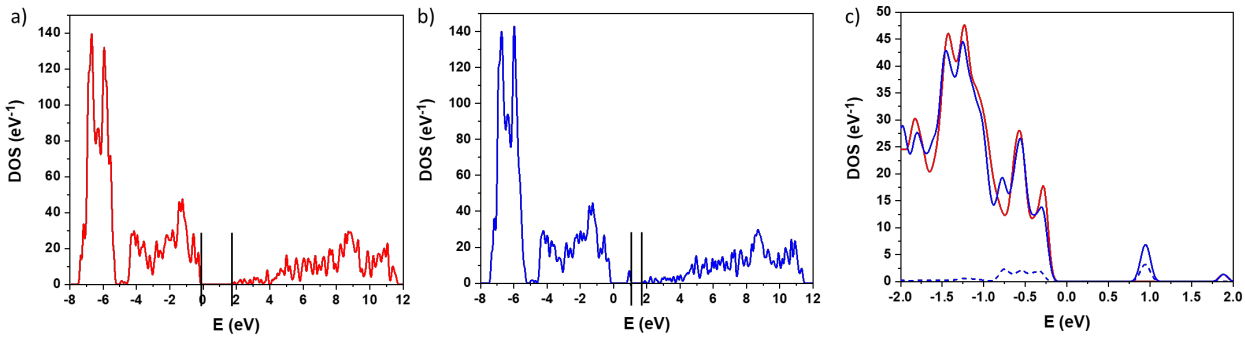

Figure 9. Total DOS for (a) pure ZnO and (b) $ZnS_x@ZnO_{1-x}$ with a sulfidation level of 6.25 at%. Dark lines indicate the band gap. (c) Excerpt of gap zone with total DOS for ZnO (in red), $ZnS_x@ZnO_{1-x}$ (blue), and for the projected DOS on the S 3p states of ZnS_xO_{1-x} (blue dotted line).

CONCLUSION

From a fundamental perspective, we investigated the controlled synthesis of $ZnS_x@ZnO_{1-x}$ semiconducting heterostructures from ZnO nanomaterial templates of well controlled shapes, originally obtained by the mild hydrolysis of the organometallic precursor $ZnCy_2$. Extensive structural characterization by PXRD and WAXS, and optical and band gap measurements related to the sulfidation ratio of isotropic NPs and NRs indicate that sulfidation mechanism takes place through the replacement of ZnO by ZnS domains, with the initially present O–vacancies acting as gateways for S–atoms. High resolution microscopy, including STEM–HAADF coupled with EDX analysis, has demonstrated that $ZnS_x@ZnO_{1-x}$ hollowing rearrangement process involves the progressive structural metamorphosis of the monocrystalline pure ZnO into polycrystalline ZnS hollow structures *via* amorphization–crystallization steps. The analysis of the local environment in these $ZnS_x@ZnO_{1-x}$ heterostructures was achieved for the first time using multinuclear NMR spectroscopy (^{1}H, ^{13}C, ^{17}O). The extensive quantitative data of the sulfidation kinetics allowed us to differentiate the surface and core O–atoms. In particular, it was possible to characterize and quantify the O–

atoms at the interfaces between the ZnO and ZnS zones as a function of the level of sulfidation. Those O–atoms are more easily exchanged during isotopic–exchange measurements compared to O–atoms at the core of the ZnO domains, suggesting a greater mobility of the O–atoms at the interfaces. The ^{17}O NMR analysis combined with the HR–TEM highlighted important aspects concerning the sulfidation mechanism of ZnO nanoparticles towards well–controlled $ZnS_x@ZnO_{1-x}$ heterostructures. Oxygen vacancies initially present serve as preferential gateways for the incoming sulfur atoms and constitute a powerful driving force of the sulfidation process. Thus, a decisive issue for controlling the anion exchange–process is the identification and quantification of these vacancies that we address in the present work using methodological NMR approach, and which allowed us to make the link between the macroscopic properties of materials and their atomic structure. The computational results of surface processes reinforced the mechanism proposed on the basis of these experimental data by reproducing the variation and trends in optical properties and the bowing of band gap as a function of sulfidation level of the $ZnS_x@ZnO_{1-x}$ heterostructures. This ion–exchange approach is flexible allowing the use of various sulfuring agents, such as H_2S or notably $(TMS)_2S$, whose strong oxygen atom extractor effect induces large scale structural modification. This global reorganization into hybrid heterostructures of tunable physicochemical properties are pertinent for studying other elaborate heterostructures of semiconducting nature.

EXPERIMENTAL SECTION

Synthesis All air–sensitive manipulations were conducted under an inert atmosphere in an argon–filled Braun LABstar Eco glovebox or by standard Schlenk technique under argon. All glassware was heated in an oven at 90 °C overnight and cooled under vacuum prior to use. Dry and oxygen–free THF used for synthesis was collected from LabSolv (Innovative Technology) solvent purification system, while anhydrous mesitylene was used without further purification. $ZnCy_2$ was stored at -20 °C in the glovebox and all other reagents were used without any further

purifications. Commercial reagents were obtained from the following vendors and used without further purification: Nanomeps: $ZnCy_2$, Acros Organics: dodecylamine (DDA), Sigma–Aldrich: $(TMS)_2S$, H_2S solution in THF (0.8 M), Eurisotop: $H_2{}^{17}O$ (35–40% ^{17}O labelled).

ZnO iNPs In a glove box, $Zn(Cy)_2$ (300 mg, 1.29 mmol) was added to a THF (20 mL) solution of DDA (240 mg, 1.29 mmol) in a Schlenk flask. After diluting the reaction mixture with additional THF (16 mL), the flask was taken outside the glove box and a stock solution of H_2O in THF (2 equiv. of H_2O in 1.0 mL of THF) was added to the reaction mixture. The reaction is left to stir at room temperature for overnight. After 16 h of reaction time, the as–obtained ZnO iNPs were used in the sulfidation reaction with suitable amount of $(TMS)_2S$ as described below.

ZnS_x@ZnO_{1-x} iNPs To the suspension of ZnO iNPs from the previous step was added outside the glove box appropriate amount of $(TMS)_2S$ (0.2, 0.5, 0.8 or 1.0 equiv.) in a dropwise manner. After the addition, the flask was left to stir for 22 h at room temperature. Upon completion of the reaction, volatiles were removed under vacuum and the product was washed with dry pentane and degassed acetone (3 × 10 mL) and centrifuged (2 × 15 min at 3500 rpm). The remaining solid was dried under vacuum to yield orange yellow to orange solid depending of the amount of $(TMS)_2S$ reagent used. All ZnS_x@ZnO_{1-x} iNP samples were washed with pentane and acetone to remove the excess of DDA. This washing facilitates the sample manipulation because after the washings, the sample evolves from a sticky paste to a fine powder. Note that the formation of disulfide $(S_2)^{2-}$ bonds are not to be expected to form under the very mild reaction conditions used herein.

ZnO NRs In a glove box, $Zn(Cy)_2$ (300 mg, 1.29 mmol) and DDA (2 equiv., 480 mg, 2.59 mmol) were weighed into a small vial and the latter was placed inside a larger vial equipped with a septum. The setup was transferred outside the glove box and degassed H_2O (4 equiv., 93 μL, 5.18 mmol) was added via syringe to the larger vial, while taking careful precaution to

avoid direct contact with the content of the smaller vial. The setup was wrapped with aluminium foil and the reaction mixture was left to stand at room temperature for four days.

ZnS_x@ZnO_{1-x} NRs The obtained ZnO NRs (1.29 mmol) from the previous step were dispersed in THF (12 mL) in a Schlenk flask equipped with a magnetic stirring bar. After taking the flask outside the glove box, appropriate amount of $(TMS)_2S$ (0.2, 0.5, 0.8 or 1.0 equiv.) was added dropwise and afterwards the flask was left to stir for 22 h at room temperature. Upon completion of the reaction, volatiles were removed under vacuum and the product was washed with dry pentane and degassed acetone (3 × 10 mL) and centrifuged (2 × 15 min at 3500 rpm). The remaining product was dried under vacuum to yield orange yellow to orange solid depending of the amount of $(TMS)_2S$ reagent used. All ZnS_x@ZnO_{1-x} NR samples were washed with pentane and acetone to remove the excess of DDA. This washing facilitates the sample manipulation because after the washings, the sample evolves from a sticky paste to a fine powder.

ZnS_x@$Zn^{17}O_{1-x}$ iNPs or NRs The synthesis of ^{17}O–labelled heterostructures were carried out the same way as described above, except using $H_2{}^{17}O$ (35–40% ^{17}O labelled) instead of H_2O.

ASSOCIATED CONTENT

Supporting Information.

This material is available free of charge via the Internet at http://pubs.acs.org. Experimental conditions for labelling studies of ZnS_x@ZnO_{1-x}; optical spectra; TEM images of NRs and iNPs; 2D, size distribution and aspect ratio plots; EDX analysis; DRX and WAXS spectra; $^1H \rightarrow {}^{13}C$ CP-MAS spectra of DDA, ZnS_x@ZnO_{1-x}·DDA NRs and iNPs; ^{17}O MQMAS, ^1H and ^{17}O MAS NMR spectra; computational details.

AUTHOR INFORMATION

Corresponding Authors

Myrtil L. Kahn – *LCC–CNRS, Université de Toulouse, CNRS, UPS, Toulouse 31077, France;* orcid.org/0000-0003-3079-5759; Email: myrtil.kahn@lcc-toulouse.fr

Authors

Ekaterina Bellan – *LCC–CNRS, Université de Toulouse, CNRS, UPS, Toulouse 31077, France;*

Martin Jakoobi – *LCC–CNRS, Université de Toulouse, CNRS, UPS, Toulouse 31077, France;*

orcid.org/0000-0002-6181-4839

Vincent Collière – *LCC–CNRS, Université de Toulouse, CNRS, UPS, Toulouse 31077, France;*

orcid.org/0000-0003-1937-6991

Yannick Coppel – *LCC–CNRS, Université de Toulouse, CNRS, UPS, Toulouse 31077, France;* orcid.org/0000-0003-0970-4082

Julien Trébosc – Univ. Lille, CNRS, INRAE, Centrale Lille, Univ. Artois, FR 2638 − IMEC − Institut Michel-Eugène Chevreul, F-59000 Lille, France. orcid.org/0000-0002-4034-855X

Olivier Lafon – Univ. de Lille, CNRS, Centrale Lille, Univ. Artois, UMR 8181 − UCCS – Unité de Catalyse et Chimie du Solide, F-59000 Lille, France; orcid.org/0000-0002-5214

Pierre Lecante – *CEMES, UPS, Toulouse 31055, France*

Pierre Fau – *LCC–CNRS, Université de Toulouse, CNRS, UPS, Toulouse 31077, France;* orcid.org/0000-0003-0014-2511

Katia Fajerwerg – *LCC–CNRS, Université de Toulouse, CNRS, UPS, Toulouse 31077, France;* orcid.org/0000-0002-3897-3380

Paul Fleurat–Lessard – Institut de Chimie Moléculaire de l'Université de Bourgogne UMR6302, CNRS, Univ. Bourgogne, 9 avenue Alain Savary, 21000 Dijon, France orcid.org/0000-0003-3114-2522

Céline Dupont – Laboratoire Interdisciplinaire Carnot de Bourgogne (ICB), Université de Bourgogne (uB), 9 avenue Alain Savary BP 47870, 21078 Dijon, France orcid.org/0000-0001-5291-7011

Jean–Cyrille Hierso – Institut de Chimie Moléculaire de l'Université de Bourgogne UMR6302, CNRS, Univ. Bourgogne, 9 avenue Alain Savary, 21000 Dijon, France orcid.org/0000-0002-2048-647X

Lauriane Pautrot–d'Alençon – *Solvay, Research and Innovation Centre de Paris, Aubervilliers 93308, France;*

Thierry Le Mercier – *Solvay, Research and Innovation Centre de Paris, Aubervilliers 93308, France;*

Present Addresses

† Current address of Ekaterina Bellan is Solvay, Research and Innovation Center de Paris, 52 rue de La Haie Coq, Aubervilliers 93308, France.

Author Contributions

L. D'A., T. L. M., and M. L. K conceived this program. E. B. and M. J. synthesized the materials. K. F. and P. F. participated in the characterization of materials. P. L. analyzed the XRD measurements. Y. C., J.T. and O. L. performed and analyzed the NMR experiments. P. F.–L. and C. D. did the DFT calculations and J.–C. H. participated in the analysis of the results.

M. L. K, M. J., J.–C. H. and Y. C. wrote the manuscript. All authors valuably contributed to the discussions and approved the final version of the manuscript.

Funding Sources

The work was supported by the CNRS, Ministère de l'Enseignement Supérieur et de la Recherche. J. L. and O. L. thank the Chevreul Institute for supporting CPER projects funded by the "Ministère de l'Enseignement Supérieur et de la Recherche", the region "Hauts-de-France", the ERDF program of the European Union and the "Métropole Européenne de Lille". Financial support from the IR INFRANALYTICS FR2054 for conducting the research is gratefully acknowledged. Authors are also grateful for funding supported by contract ANR-22-CE29-0007-01 (IVAN). K. F. and P. F. are grateful for funding provided by the Université de Toulouse. Calculations were performed using HPC resources from DNUM CCUB (Centre de Calcul de l'Université de Bourgogne).

The authors declare no competing financial interest.

ABBREVIATIONS

NPs; nanoparticles; NC; nanocrystal; iNPs; isotropic nanoparticles; NMR; nuclear magnetic resonance; DDA; dodecylamine; PXRD; powder X–ray diffraction; RDF; Radial distribution function;

REFERENCES

(1) Vattikuti, S. V. P. Chapter 4 - Heterostructured Nanomaterials: Latest Trends in Formation of Inorganic Heterostructures. In *Synthesis of Inorganic Nanomaterials*; Mohan Bhagyaraj, S., Oluwafemi, O. S., Kalarikkal, N., Thomas, S., Eds.; Woodhead Publishing, 2018; pp 89–120. https://doi.org/10.1016/B978-0-08-101975-7.00004-X.
(2) Lalwani, S.; AlNahyan, M.; Al Zaabi, A.; AlMarzooqi, F.; Qurashi, A. Advances in Interfacial Engineering and Their Role in Heterostructure Formation for HER

Applications in Wider pH. *ACS Appl. Energy Mater.* **2022**, *5* (12), 14571–14592. https://doi.org/10.1021/acsaem.2c02102.
(3) Yang, X.; Liu, H.; Li, T.; Huang, B.; Hu, W.; Jiang, Z.; Chen, J.; Niu, Q. Preparation of Flower-like ZnO@ZnS Core-Shell Structure Enhances Photocatalytic Hydrogen Production. *Int. J. Hydrog. Energy* **2020**, *45* (51), 26967–26978. https://doi.org/10.1016/j.ijhydene.2020.07.027.
(4) Tahir, M.; Tasleem, S.; Tahir, B. Recent Development in Band Engineering of Binary Semiconductor Materials for Solar Driven Photocatalytic Hydrogen Production. *Int. J. Hydrog. Energy* **2020**, *45* (32), 15985–16038. https://doi.org/10.1016/j.ijhydene.2020.04.071.
(5) Xiao, L.; Lin, R.; Wang, J.; Cui, C.; Wang, J.; Li, Z. A Novel Hollow-Hierarchical Structured Bi_2WO_6 with Enhanced Photocatalytic Activity for CO_2 Photoreduction. *J. Colloid Interface Sci.* **2018**, *523*, 151–158. https://doi.org/10.1016/j.jcis.2018.03.064.
(6) Avansi, W. Jr.; Catto, A. C.; da Silva, L. F.; Fiorido, T.; Bernardini, S.; Mastelaro, V. R.; Aguir, K.; Arenal, R. One-Dimensional V_2O_5/TiO_2 Heterostructures for Chemiresistive Ozone Sensors. *ACS Appl. Nano Mater.* **2019**, *2* (8), 4756–4764. https://doi.org/10.1021/acsanm.9b00578.
(7) Chu, S.; Yang, C.; Su, X. Synthesis of NiO Hollow Nanospheres via Kirkendall Effect and Their Enhanced Gas Sensing Performance. *Appl. Surf. Sci.* **2019**, *492*, 82–88. https://doi.org/10.1016/j.apsusc.2019.06.226.
(8) Yang, R.; Wang, F.; Lu, J.; Lu, Y.; Lu, B.; Li, S.; Ye, Z. ZnO with P-Type Doping: Recent Approaches and Applications. *ACS Appl. Electron. Mater.* **2023**, *5* (8), 4014–4034. https://doi.org/10.1021/acsaelm.3c00515.
(9) Shulenberger, K. E.; Jilek, M. R.; Sherman, S. J.; Hohman, B. T.; Dukovic, G. Electronic Structure and Excited State Dynamics of Cadmium Chalcogenide Nanorods. *Chem. Rev.* **2023**, *123* (7), 3852–3903. https://doi.org/10.1021/acs.chemrev.2c00676.
(10) Chong, W.-K.; Ng, B.-J.; Tan, L.-L.; Chai, S.-P. Recent Advances in Nanoscale Engineering of Ternary Metal Sulfide-Based Heterostructures for Photocatalytic Water Splitting Applications. *Energy Fuels* **2022**, *36* (8), 4250–4267. https://doi.org/10.1021/acs.energyfuels.2c00291.
(11) Shu, J.; Tang, D. Recent Advances in Photoelectrochemical Sensing: From Engineered Photoactive Materials to Sensing Devices and Detection Modes. *Anal. Chem.* **2020**, *92* (1), 363–377. https://doi.org/10.1021/acs.analchem.9b04199.
(12) Ye, L.; Xu, X.; He, S.; Liu, Y.; Jin, Y.; Yang, Y. M.; Zhu, H. Molecular Triplet Sensitization of Monolayer Semiconductors in 2D Organic/Inorganic Hybrid Heterostructures. *ACS Nano* **2022**, *16* (8), 12532–12540. https://doi.org/10.1021/acsnano.2c03995.
(13) Zhang, T.; Fujisawa, K.; Zhang, F.; Liu, M.; Lucking, M. C.; Gontijo, R. N.; Lei, Y.; Liu, H.; Crust, K.; Granzier-Nakajima, T.; Terrones, H.; Elías, A. L.; Terrones, M. Universal In Situ Substitutional Doping of Transition Metal Dichalcogenides by Liquid-Phase Precursor-Assisted Synthesis. *ACS Nano* **2020**, *14* (4), 4326–4335. https://doi.org/10.1021/acsnano.9b09857.
(14) Hao, L.; Huang, H.; Zhang, Y.; Ma, T. Oxygen Vacant Semiconductor Photocatalysts. *Adv. Funct. Mater.* **2021**, *31* (25), 2100919. https://doi.org/10.1002/adfm.202100919.
(15) Pham, P. V.; Bodepudi, S. C.; Shehzad, K.; Liu, Y.; Xu, Y.; Yu, B.; Duan, X. 2D Heterostructures for Ubiquitous Electronics and Optoelectronics: Principles, Opportunities, and Challenges. *Chem. Rev.* **2022**, *122* (6), 6514–6613. https://doi.org/10.1021/acs.chemrev.1c00735.
(16) Yoon, Y. J.; Biesold, G.; Liang, S.; Wang, Z.; Harn, Y. W.; Lu, C.-H.; Kim, R.; Yao, W.; Lane, S.; James, J. C.; Ding, Y.; Lin, Z.; Kang, Z. Stable Infrared-Emitting Chemical

Composition Gradient Quantum Dots for Down-Convertors and Photodetectors. *ACS Appl. Nano Mater.* **2020**, *3* (11), 11335–11343. https://doi.org/10.1021/acsanm.0c02434.
(17) Min, Y.; Kwak, J.; Soon, A.; Jeong, U. Nonstoichiometric Nucleation and Growth of Multicomponent Nanocrystals in Solution. *Acc. Chem. Res.* **2014**, *47* (10), 2887–2893. https://doi.org/10.1021/ar500133w.
(18) Drake, G. A.; Keating, L. P.; Shim, M. Design Principles of Colloidal Nanorod Heterostructures. *Chem. Rev.* **2023**, *123* (7), 3761–3789. https://doi.org/10.1021/acs.chemrev.2c00410.
(19) Wang, S.; Liao, W.; Su, H.; Pang, S.; Yang, C.; Fu, Y.; Zhang, Y. Review on the Application of Semiconductor Heterostructures in Photocatalytic Hydrogen Evolution: State-of-the-Art and Outlook. *Energy Fuels* **2023**, *37* (3), 1633–1656. https://doi.org/10.1021/acs.energyfuels.2c03429.
(20) Qiao, F.; Sun, K.; Liu, W.; Xie, Y.; Chu, H. Bandgap Modulation of ZnO/ZnS Heterostructures through Ion Exchange and Their Efficient Transport Properties. *Vacuum* **2022**, *196*, 110788. https://doi.org/10.1016/j.vacuum.2021.110788.
(21) Guo, C.; Wang, Q.; He, J.; Wu, C.; Xie, K.; Liu, Y.; Zhang, W.; Cheng, H.; Hu, H.; Wang, C. Rational Design of Unique ZnO/ZnS@N-C Heterostructures for High-Performance Lithium-Ion Batteries. *J. Phys. Chem. Lett.* **2020**, *11* (3), 905–912. https://doi.org/10.1021/acs.jpclett.9b03677.
(22) Ma, B.; Zhang, C.; Jia, D.; Zhao, Q.; Yang, P. NiAl-LDH-Modified Core–Shell Rod-like ZnO@ZnS Heterostructures for Enhanced Photocatalytic Hydrogen Precipitation. *J. Phys. Chem. C* **2023**, *127* (6), 2908–2917. https://doi.org/10.1021/acs.jpcc.2c07734.
(23) Fareza, A. R.; Nugroho, F. A. A.; Fauzia, V. One-Step Coating of a ZnS Nanoparticle/MoS_2 Nanosheet Composite on Supported ZnO Nanorods as Anodes for Photoelectrochemical Water Splitting. *ACS Appl. Nano Mater.* **2022**, *5* (11), 16051–16060. https://doi.org/10.1021/acsanm.2c01434.
(24) Larquet, C.; Carenco, S. Metal Oxysulfides: From Bulk Compounds to Nanomaterials. *Front. Chem.* **2020**, *8*, 179. https://doi.org/10.3389/fchem.2020.00179.
(25) Fu, Y.; Gledhill, S.; Fischer, C.-H. Mechanistic Study of the Gas-Phase Chemistry during the Spray Deposition of Zn(O,S) Films by Mass Spectrometry. *Ultrason. Sonochem.* **2021**, *73*, 105492. https://doi.org/10.1016/j.ultsonch.2021.105492.
(26) Wang, C.; Liu, H.; Zhou, G.; Li, T. Templated Synthesis and Photocatalytic Activity of ZnO/ZnS Heterojunction. *Russ. J. Phys. Chem. A* **2018**, *92* (1), 200–203. https://doi.org/10.1134/S0036024418010302.
(27) Bao, D.; Gao, P.; Zhu, X.; Sun, S.; Wang, Y.; Li, X.; Chen, Y.; Zhou, H.; Wang, Y.; Yang, P. ZnO/ZnS Heterostructured Nanorod Arrays and Their Efficient Photocatalytic Hydrogen Evolution. *Chem. – Eur. J.* **2015**, *21* (36), 12728–12734. https://doi.org/10.1002/chem.201501595.
(28) Lim, Y.; Lee, C.-H.; Jun, C.-H.; Kim, K.; Cheon, J. Morphology-Conserving Non-Kirkendall Anion Exchange of Metal Oxide Nanocrystals. *J. Am. Chem. Soc.* **2020**, *142* (20), 9130–9134. https://doi.org/10.1021/jacs.0c03230.
(29) Park, J.; Zheng, H.; Jun, Y.; Alivisatos, A. P. Hetero-Epitaxial Anion Exchange Yields Single-Crystalline Hollow Nanoparticles. *J. Am. Chem. Soc.* **2009**, *131* (39), 13943–13945. https://doi.org/10.1021/ja905732q.
(30) Kozhevnikova, N. S.; Gyrdasova, O. I.; Vorokh, A. S.; Melkozerova, M. A.; Bamburov, V. G. Synthesis and Defect Structure of Quasi-One-Dimensional Composite Material ZnO/ZnS. *Dokl. Chem.* **2017**, *474* (1), 116–120. https://doi.org/10.1134/S0012500817050056.
(31) Kumari, P.; Pande, S.; Fageria, P. Facile Synthesis of ZnO/ZnS Hollow Nanorods via Kirkendall Effect with Enhanced Photocatalytic Degradation of Methylene Blue.

Environ. Sci. Pollut. Res. **2023**, *30* (22), 61927–61944. https://doi.org/10.1007/s11356-023-26192-1.
(32) Ma, X.; Zheng, J.; Jin, H.; Zeng, X.; Li, D.; You, F.; Qi, J.; Yuan, F. Deep Understanding the Formation of Hollow ZnO@ZnS Core-Sheath Heterojunction towards Efficient CO_2 Photoreduction. *Sep. Purif. Technol.* **2024**, *329*, 125228. https://doi.org/10.1016/j.seppur.2023.125228.
(33) Hong, Y.-K.; Park, Y.; Kang, H.; Son, H.; Ha, D.-H. Nanoparticle Transformation from ZnO to ZnS through Anion Exchange with Di-Tert-Butyl Disulphide. *Dalton Trans.* **2021**, *50* (6), 2192–2199. https://doi.org/10.1039/D0DT03940C.
(34) Wang, W.; Dahl, M.; Yin, Y. Hollow Nanocrystals through the Nanoscale Kirkendall Effect. *Chem. Mater.* **2013**, *25* (8), 1179–1189. https://doi.org/10.1021/cm3030928.
(35) Smigelskas, Alice. D.; Kirkendall, Ernest. O. Zinc Diffusion in Alpha Brass. *Trans AIME* **1947**, *171*, 130–142.
(36) Pandey, S. K.; Pandey, S.; Parashar, V.; Yadav, R. S.; Mehrotra, G. K.; Pandey, A. C. Bandgap Engineering of Colloidal Zinc Oxysulfide via Lattice Substitution with Sulfur. *Nanoscale* **2014**, *6* (3), 1602–1606. https://doi.org/10.1039/C3NR04457B.
(37) Gross, S.; Vittadini, A.; Dengo, N. Functionalisation of Colloidal Transition Metal Sulphides Nanocrystals: A Fascinating and Challenging Playground for the Chemist. *Crystals* **2017**, *7* (4). https://doi.org/10.3390/cryst7040110.
(38) Macary, L. S.; Kahn, M. L.; Estournès, C.; Fau, P.; Trémouilles, D.; Bafleur, M.; Renaud, P.; Chaudret, B. Size Effect on Properties of Varistors Made From Zinc Oxide Nanoparticles Through Low Temperature Spark Plasma Sintering. *Adv. Funct. Mater.* **2009**, *19* (11), 1775–1783. https://doi.org/10.1002/adfm.200801067.
(39) Ryzhikov, A.; Jońca, J.; Kahn, M.; Fajerwerg, K.; Chaudret, B.; Chapelle, A.; Ménini, P.; Shim, C. H.; Gaudon, A.; Fau, P. Organometallic Synthesis of ZnO Nanoparticles for Gas Sensing: Towards Selectivity through Nanoparticles Morphology. *J. Nanoparticle Res.* **2015**, *17* (7), 280. https://doi.org/10.1007/s11051-015-3086-2.
(40) Jońca, J.; Ryzhikov, A.; Kahn, M. L.; Fajerwerg, K.; Chapelle, A.; Menini, P.; Fau, P. SnO2 “Russian Doll” Octahedra Prepared by Metalorganic Synthesis: A New Structure for Sub-Ppm CO Detection. *Chem. – Eur. J.* **2016**, *22* (29), 10127–10135. https://doi.org/10.1002/chem.201600650.
(41) Jońca, J.; Ryzhikov, A.; Palussière, S.; Esvan, J.; Fajerwerg, K.; Menini, P.; Kahn, M. L.; Fau, P. Organometallic Synthesis of CuO Nanoparticles: Application in Low-Temperature CO Detection. *ChemPhysChem* **2017**, *18* (19), 2658–2665. https://doi.org/10.1002/cphc.201700693.
(42) Spataro, G.; Dazzazi, A.; Fortuny, S.; Champouret, Y.; Coppel, Y.; Rubio-Garcia, J.; Bouhaouss, A.; Gauffre, F.; Kahn, M. L. Insight into the Role of Ligands in the Yellow Luminescence of Zinc Oxide Nanocrystals. *Eur. J. Inorg. Chem.* **2016**, *2016* (13–14), 2056–2062. https://doi.org/10.1002/ejic.201501186.
(43) Bellan, E.; Maleki, F.; Jakoobi, M.; Fau, P.; Fajerwerg, K.; Lagarde, D.; Balocchi, A.; Lecante, P.; Trébosc, J.; Xu, Y.; Gan, Z.; Pautrot-d’Alençon, L.; Le Mercier, T.; Nagashima, H.; Pacchioni, G.; Lafon, O.; Coppel, Y.; Kahn, M. L. Ultra-High-Field ^{67}Zn and ^{33}S NMR Studies Coupled with DFT Calculations Reveal the Structure of ZnS Nanoplatelets Prepared by an Organometallic Approach. *J. Phys. Chem. C* **2023**, *127* (36), 17809–17819. https://doi.org/10.1021/acs.jpcc.3c02754.
(44) Kahn, M. L.; Glaria, A.; Pages, C.; Monge, M.; Saint Macary, L.; Maisonnat, A.; Chaudret, B. Organometallic Chemistry: An Alternative Approach towards Metal Oxide Nanoparticles. *J. Mater. Chem.* **2009**, *19* (24), 4044–4060. https://doi.org/10.1039/B818935H.

(45) Champouret, Y.; Spataro, G.; Coppel, Y.; Gauffre, F.; Kahn, M. L. Nanocrystal–Ligand Interactions Deciphered: The Influence of HSAB and pKa in the Case of Luminescent ZnO. *Nanoscale Adv.* **2020**, *2* (3), 1046–1053. https://doi.org/10.1039/C9NA00769E.
(46) Wei, S.-H.; Ferreira, L. G.; Bernard, J. E.; Zunger, A. Electronic Properties of Random Alloys: Special Quasirandom Structures. *Phys. Rev. B* **1990**, *42* (15), 9622–9649. https://doi.org/10.1103/PhysRevB.42.9622.
(47) Wei, S.; Zunger, A. Band Offsets and Optical Bowings of Chalcopyrites and Zn-based II-VI Alloys. *J. Appl. Phys.* **1995**, *78* (6), 3846–3856. https://doi.org/10.1063/1.359901.
(48) Meyer, B. K.; Polity, A.; Farangis, B.; He, Y.; Hasselkamp, D.; Krämer, Th.; Wang, C. Structural Properties and Bandgap Bowing of ZnO1−xSx Thin Films Deposited by Reactive Sputtering. *Appl. Phys. Lett.* **2004**, *85* (21), 4929–4931. https://doi.org/10.1063/1.1825053.
(49) The Urbach energy, or Urbach edge, is a parameter with dimensions of energy, used to quantify energetic disorder in the band edges of a semiconductor. For further details, see reference "Kurik, M. V., Physica Status Solidi A. 1971, 8, 9–45".
(50) Seo, K.; Suh, M.; Ju, S. Control of Oxygen Vacancy Concentration in ZnO Nanowires Containing Sulfur as a Reducing Agent. *Electron. Mater. Lett.* **2013**, *9* (3), 273–277. https://doi.org/10.1007/s13391-013-2176-5.
(51) Zhao, Z.; Zheng, Z.; Roux, C.; Delmas, C.; Marty, J.-D.; Kahn, M. L.; Mingotaud, C. Importance of the Correlation between Width and Length in the Shape Analysis of Nanorods: Use of a 2D Size Plot To Probe Such a Correlation. *Chem. – Eur. J.* **2016**, *22* (35), 12424–12429. https://doi.org/10.1002/chem.201601837.
(52) These mean diameters are evaluated by fitting of the histogram with a Gaussian curve. The first value corresponds to the center of the peak whereas the second one corresponds to twice the standard deviation of the Gaussian distribution or approximately 0.849 the width of the peak at half–height.
(53) In statistics, the Pearson correlation coefficient (PCC) is a correlation coefficient that measures linear correlation between two sets of data. It is the ratio between the covariance of two variables and the product of their standard deviations; thus, it is essentially a normalized measurement of the covariance, such that the result always has a value between −1 and 1. For further details, see reference: Regression and Inheritance in the Case of Two Parents, Karl Pearson, Proceedings of the Royal Society of London, 1895, 58, 240-242.
(54) Choi, W.; Park, G.; Bae, K.-L.; Choi, J. Y.; Seo, W. S.; Nam, K. M.; Song, H. Metal–CdSe Double Shell Hollow Nanocubes via Sequential Nanoscale Reactions and Their Photocatalytic Hydrogen Evolution. *Top. Catal.* **2018**, *61* (9), 965–976. https://doi.org/10.1007/s11244-018-0951-0.
(55) Saha, M.; Ghosh, S.; De, S. K. Nanoscale Kirkendall Effect Driven Au Decorated CdS/CdO Colloidal Nanocomposites for Efficient Hydrogen Evolution, Photocatalytic Dye Degradation and Cr (VI) Reduction. *SI Adv. Photocatal.* **2020**, *340*, 253–267. https://doi.org/10.1016/j.cattod.2018.11.027.
(56) Widdifield, C. M.; Kaur, N. 9.15 - NMR of Nanoparticles. In *Comprehensive Inorganic Chemistry III (Third Edition)*; Reedijk, J., Poeppelmeier, K. R., Eds.; Elsevier: Oxford, 2023; pp 398–449. https://doi.org/10.1016/B978-0-12-823144-9.00035-2.
(57) Spataro, G.; Champouret, Y.; Florian, P.; Coppel, Y.; Kahn, M. L. Multinuclear Solid-State NMR Study: A Powerful Tool for Understanding the Structure of ZnO Hybrid Nanoparticles. *Phys. Chem. Chem. Phys.* **2018**, *20* (18), 12413–12421. https://doi.org/10.1039/C8CP01096J.

(58) Champouret, Y.; Coppel, Y.; Kahn, M. L. Evidence for Core Oxygen Dynamics and Exchange in Metal Oxide Nanocrystals from In Situ ^{17}O MAS NMR. *J. Am. Chem. Soc.* **2016**, *138* (50), 16322–16328. https://doi.org/10.1021/jacs.6b08769.
(59) Lee, D.; Wolska-Pietkiewicz, M.; Badoni, S.; Grala, A.; Lewiński, J.; De Paëpe, G. Disclosing Interfaces of ZnO Nanocrystals Using Dynamic Nuclear Polarization: Sol-Gel versus Organometallic Approach. *Angew. Chem. Int. Ed.* **2019**, *58* (48), 17163–17168. https://doi.org/10.1002/anie.201906726.
(60) Using the $^{1}H \rightarrow ^{13}C$ CPMAS experiment for precise quantification of the degree of sulfidation would require a more detailed study by measuring CP build-up curves and changing the number of ligand equivalents, which is beyond the scope of this study.
(61) Nagashima, H.; Trébosc, J.; Kon, Y.; Sato, K.; Lafon, O.; Amoureux, J.-P. Observation of Low-γ Quadrupolar Nuclei by Surface-Enhanced NMR Spectroscopy. *J. Am. Chem. Soc.* **2020**, *142* (24), 10659–10672. https://doi.org/10.1021/jacs.9b13838.
(62) Nagashima, H.; Maleki, F.; Trébosc, J.; Belgamwar, R.; Polshettiwar, V.; Kahn, M.; Kon, Y.; Pacchioni, G.; Lafon, O.; Amoureux, J.-P. Probing the Surface of Oxide Nanoparticles Using DNP-Enhanced High-Resolution NMR of Quadrupolar Nuclei. *J. Phys. Chem. Lett.* **2024**, *15* (18), 4858–4863. https://doi.org/10.1021/acs.jpclett.4c00563.
(63) Song, B.; Li, Y.; Wu, X.-P.; Wang, F.; Lin, M.; Sun, Y.; Jia, A.; Ning, X.; Jin, L.; Ke, X.; Yu, Z.; Yang, G.; Hou, W.; Ding, W.; Gong, X.-Q.; Peng, L. Unveiling the Surface Structure of ZnO Nanorods and H_2 Activation Mechanisms with ^{17}O NMR Spectroscopy. *J. Am. Chem. Soc.* **2022**, *144* (51), 23340–23351. https://doi.org/10.1021/jacs.2c08356.
(64) Bastow, T. J.; Stuart, S. N. ^{17}O NMR in Simple Oxides. *Chem. Phys.* **1990**, *143* (3), 459–467. https://doi.org/10.1016/0301-0104(90)87025-7.
(65) Chen, K. A Practical Review of NMR Lineshapes for Spin-1/2 and Quadrupolar Nuclei in Disordered Materials. *Int. J. Mol. Sci.* **2020**, *21* (16). https://doi.org/10.3390/ijms21165666.

SYNOPSIS

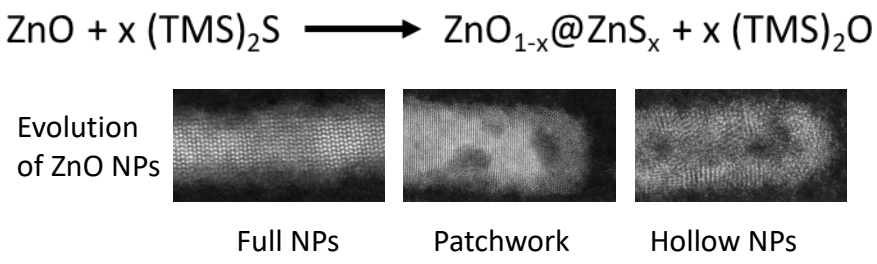
ZnO + x (TMS)2S
ZnO1-x@ZnSx + x (TMS)2O
Evolution of ZnO NPs
Full NPs
Patchwork
Hollow NPs